J. Fluid Mech. (2014), *vol.* 741, *pp* 280–315.
doi:10.1017/jfm.2013.677

Streak instabilities in boundary layers beneath free-stream turbulence

M. J. P. Hack and T. A. Zaki†

Department of Mechanical Engineering, Imperial College, London SW7 2AZ, UK

(Received 1 April 2013; revised 3 December 2013; accepted 18 December 2013; first published online 13 February 2014)

The secondary instability of boundary layer streaks is investigated by means of direct stability analysis. The base flow is computed in direct simulations of bypass transition. The random nature of the free-stream perturbations causes the formation of a spectrum of streaks inside the boundary layer, with breakdown to turbulence initiated by the amplification of localized instabilities of individual streaks. The capability of the instability analysis to predict the instabilities which are observed in the direct numerical simulation is established. Furthermore, the analysis is shown to identify the particular streaks that break down to turbulence farther downstream. Two particular configurations of streaks regularly induce the growth of these localized instabilities: low-speed streaks that are lifted towards the edge of the boundary layer, and the local overlap between high-speed and low-speed streaks inside the boundary layer. It is established that the underlying modes can be ascribed to the general classification of inner and outer modes which was introduced by Vaughan & Zaki (*J. Fluid Mech.*, vol. 681, 2011, pp. 116–153). Statistical evaluations show that Blasius boundary layers favour the amplification of outer instabilities. Adverse pressure gradient promotes breakdown to turbulence via the inner mode.

Key words: boundary layer stability, transition to turbulence

1. Introduction

Exposure of a laminar boundary layer to vortical free-stream disturbances induces a rapid breakdown to turbulence in which the Tollmien–Schlichting (TS) instability is bypassed. Instead, elongated perturbations commonly referred to as streaks, which are dominated by the streamwise velocity component, are generated inside the boundary layer. The amplitude of these streaks significantly exceeds that of the free-stream perturbations. The resulting modulation of the velocity profile renders the streaky boundary layer susceptible to secondary instabilities. These instabilities are high frequency, have substantially larger growth rates than TS waves and lead to rapid breakdown to turbulence (for recent reviews of bypass transition, see Durbin & Wu (2007) and Zaki (2013)). The ability to predict the onset of secondary instability of the streaky boundary layer, in realistic flow configurations, is the focus of the current work. The computed instabilities are described in detail and related to the literature which to date has only considered idealized streaks.

†Present address: Department of Mechanical Engineering, Johns Hopkins University, Baltimore, MD 21218, USA. Email address for correspondence: t.zaki@imperial.ac.uk

The amplification of boundary-layer streaks, often referred to as Klebanoff distortions, is well understood. The 'lift-up' mechanism described by Landahl (1975, 1980) attributes streaks to the vertical displacement of mean momentum inside the boundary layer. This 'algebraic' amplification mechanism leads to energy growth which is followed by viscous decay, and is thus often referred to as transient growth. The process is non-modal and is therefore independent of the linear stability of the base flow (Hultgren & Gustavsson 1981; Trefethen *et al.* 1993). In bypass transition beneath free-stream turbulence, a mechanism is required to relate the free-stream disturbance to the generation of streaks inside the mean shear.

Studies by Jacobs & Durbin (1998) and later by Zaki & Saha (2009) compared the diffusive time scale of free-stream vortical disturbances to the mean-shear time scale, and demonstrated a filtering effect of the boundary layer. Only low-frequency free-stream disturbances can penetrate the shear: a phenomenon known as 'shear sheltering' (Hunt & Carruthers 1990). These streamwise-elongated perturbations are also the most effective in causing the formation of streaks via non-modal, or algebraic growth (Gustavsson 1991; Butler & Farrell 1992). In contrast to TS waves, non-modal growth is active for all Reynolds numbers in spatial boundary layers as demonstrated by the optimal growth studies of Andersson, Berggren & Henningson (1999) and Luchini (2000). In accordance with the experiments of Westin *et al.* (1994), these works were further able to predict that the spanwise perturbation wavelength which leads to the streaks of highest amplitude is of the order of the boundary-layer thickness.

While streaks are a central element of bypass breakdown, these low-frequency flow features do not immediately trigger the nonlinear processes associated with the formation of turbulent spots (Klebanoff 1971). Streaks rather distort the boundary-layer profile, and thereby make the flow susceptible to the development of high-frequency secondary instabilities. In flow visualizations, these instabilities often become manifest in streamwise meandering of the boundary-layer streaks (Asai, Minagawa & Nishioka 2002; Mandal, Venkatakrishnan & Dey 2010). Both varicose and sinuous modes of instabilities can be identified, which respectively correspond to a spanwise symmetric and antisymmetric deformation of the base streak as originally demonstrated by Swearingen & Blackwelder (1987) in the context of Görtler vortices.

Results from the present work indicate that the scenarios under which streaky boundary layers develop secondary instabilities can be classified into two canonical cases: (i) low-speed streaks which are lifted towards the free stream; and (ii) a near-wall instability which can emerge in the overlap between high- and low-speed streaks. Following the terminology introduced by Vaughan & Zaki (2011), the corresponding instability mode is either outer or inner type. The prevalence of either scenario depends on the parameters of the base flow.

The outer mode was identified as the dominant mechanism for streak instabilities in zero-pressure-gradient (ZPG) boundary layers in the direct simulations of bypass transition conducted by Jacobs & Durbin (2001). Making use of a similar methodology, Brandt, Schlatter & Henningson (2004) later confirmed these findings and also remarked that the majority of the streak instabilities exhibit a sinuous pattern. Zaki & Durbin (2005) demonstrated that only two free-stream modes are sufficient for reproducing breakdown to turbulence via excitation of an outer-mode instability: a low-frequency perturbation that penetrates the shear and causes the formation of the base streaks, and a high-frequency component which is sheltered but nonetheless provides the initial excitation for the growth of the outer instability. Andersson *et al.* (2001) computed the outer instability using inviscid secondary instability theory. The base streaks in their study were steady, and were obtained

from optimal growth analysis. The steady-base-flow assumption was relaxed in the work of Vaughan & Zaki (2011). They examined the secondary instability of the boundary layer when the Klebanoff streaks were generated as a response to forcing by particular low-frequency vortical modes. Their Floquet analysis was able to more accurately predict the threshold for instability. When the streak amplitude exceeded 17% of the free-stream speed, the outer mode became unstable.

The inner mode on the other hand originates from a near-wall velocity profile in certain streak configurations. In a common scenario, a local overlap of the trailing edge of a low-speed streak and the leading edge of a high-speed streak causes the wall-normal velocity profile to become inflectional, leading to the development of a predominantly varicose instability near the wall. Even though Mans *et al.* (2005) do not distinguish inner and outer instabilities, the relatively low phase speed and the position of the secondary instability close to the wall indicate that the varicose mode visualized in that work is indeed of the inner type. Similar evidence suggests an inner-mode scenario behind the breakdown in the presence of a blunt leading edge reported by Nagarajan, Lele & Ferziger (2007).

Two approaches have been widely adopted in the literature for the study of secondary instabilities of streaky boundary layers. The first focuses on linear stability analyses of idealized base flows. In these studies, the base streaks are either steady (Andersson *et al.* 2001; Ricco, Luo & Wu 2011) or are a response to harmonic forcing (Vaughan & Zaki 2011). All of these works further assume strict periodicity of the instability with respect to the spanwise coordinate. Another example in the context of pressure gradient is the work by Marquillie, Ehrenstein & Laval (2011) who investigated the flow over a curved wall. Since their flow was turbulent, they constructed a base state from the mean and an average streak profile. Based on stability analysis, Marquillie *et al.* (2011) reported a change from sinuous to varicose secondary instability with increasing pressure gradient, but did not characterize the origin of the instabilities.

A second group of studies focuses on empirical observations of instabilities of streaky shear flows in experiments and simulations. For example, the experiments by Elofsson, Kawakami & Alfredsson (1999) demonstrated that the streamwise and spanwise wavenumbers of streak instabilities in channel flow are on the same order. In boundary layers, the influence of streaks on the primary TS waves was examined by Fransson *et al.* (2005). Matsubara & Alfredsson (2001) provided a detailed time sequence of the amplification of the secondary instability of streaks themselves. By means of particle image velocimetry (PIV) and dye visualizations, Mans, de Lange & van Steenhoven (2007) investigated five sinuous streak instabilities, and characterized the associated wavelengths and amplitudes. In the context of numerical simulations, a number of studies have exploited the ability to set up flow configurations that are difficult or impossible to achieve experimentally, but that can provide unique knowledge of the transition process. For example, Zaki & Durbin (2005) studied transition to turbulence due to the interaction of two pairs of free-stream vortical modes. The simulations provided an uncluttered view of the amplification of boundary-layer streaks, their outer instability and full breakdown to turbulence. Using the same approach, Zaki & Durbin (2006) evaluated the influence of pressure gradient. Both efforts did not involve any stability analyses and, by virtue of the simulation set-up, could only examine outer streak breakdown. Further phenomenological studies were performed by Liu, Zaki & Durbin (2008*a*,*b*) who simulated the interaction of TS waves and boundary-layer streaks, and by Brandt & de Lange (2008) who artificially created streak collisions which led to breakdown to turbulence.

In summary, previous efforts have led to material advancements in the understanding of secondary instabilities of streaky boundary layers. Theoretical studies have attempted to characterize the stability of increasingly realistic base states. These base flows have nonetheless remained idealized states, often obtained from the boundary-layer response to a specific well-defined forcing, for example a streamwise vortex (Andersson *et al.* 2001) or a monochromatic vortical disturbance (Vaughan & Zaki 2011). The streaks were therefore strictly periodic in the spanwise direction, and their instability was, in a sense, a collective instability of the entire row of streaks. In contrast, boundary layers beneath free-stream turbulence are laden with streaks that have different amplitudes, sizes and orientations. In this configuration, the secondary instabilities are sporadic and localized on particular streaks.

The present work applies linear instability analysis to a boundary layer subject to broadband forcing with free-stream vortical perturbations. The main objectives are: (i) to determine whether linear theory can reliably predict the localized secondary instabilities of the streaky boundary layer in this realistic flow configuration; (ii) to characterize the possible modes of instability in bypass transition beneath free-stream turbulence, and to relate them to the general classification into inner and outer modes; and (iii) to establish the statistical relevance of these instabilities to breakdown in boundary layers with pressure gradient. Both a ZPG and an adverse-pressure-gradient (APG) case are investigated.

This paper is organized as follows: in §2, the underlying computational methods for the direct simulations and the instability analysis are described. Section 3 provides a detailed study of representative cases of an outer and an inner streak instability. Characteristic quantities obtained from the instability analyses are compared to values extracted from the direct numerical simulation (DNS) flow fields. A statistical evaluation over a large number of instabilities is reported separately for ZPG and APG boundary layers in §4, and concluding remarks are provided in §5.

2. Computational aspects

2.1. *Direct numerical simulations*

The base flow of the instability analysis is extracted from DNS of boundary layers subject to free-stream turbulence. The simulation code solves the incompressible Navier–Stokes equations with the finite-volume scheme described by Rosenfeld, Kwak & Vinokur (1991). The flow field is represented in terms of the fluxes through the faces of the control volumes. A staggered grid is used with the velocities stored at the faces of the computational volumes and the pressure stored at the centre of each volume. The convection term is advanced in time using an Adams–Bashforth scheme, and a Crank–Nicolson scheme is applied for the diffusion term. Incompressible mass conservation is enforced using the fractional step method of Kim & Moin (1985).

The methodology for simulating bypass breakdown follows the work by Jacobs & Durbin (2001), which has since been successfully adopted in a number of studies (e.g. Brandt *et al.* 2004; Schrader, Brandt & Henningson 2009; Schrader, Brandt & Zaki 2011). The simulation domain starts at distance $\tilde{x}_0$ from the leading edge. This approach circumvents the computational cost associated with simulating the leading-edge region. In the current simulations, the Reynolds number is $Re_{\delta_0} = 800$ based on the inlet boundary-layer thickness. The downstream coordinate x has its origin at the inlet of the simulation domain, $x = \tilde{x} - \tilde{x}_0$. The length, width and height of the computational domain are $600 \times 30 \times 40$. The number of grid points of the current study was set to $2048 \times 192 \times 192$ in the streamwise, spanwise and transverse

directions, respectively. The resolution is hence slightly higher than the requirements identified in the comprehensive grid refinement studies by Jacobs & Durbin (2001).

All lengths are normalized by the inlet boundary-layer thickness, δ_0, and velocities are normalized by the inlet free-stream speed, U_∞. Downstream of the inflow plane, the free-stream velocity follows a power law,

$$U_\infty(x) = Cx^{\beta_H/(2-\beta_H)}. \tag{2.1}$$

The Hartree parameter, β_H, characterizes the acceleration of the free stream and, hence, the applied pressure gradient. Two cases are considered herein: $\beta_H = 0$ for ZPG and $\beta_H = -0.14$ for APG.

For all simulations, the boundary conditions are no slip at the wall and free stress at the top of the computational domain. The desired pressure gradient is imposed through a gradual increase of the domain height with downstream distance. Periodicity is enforced in the spanwise dimension. A Blasius profile is prescribed for the mean flow at the inlet of the computational domain in both ZPG and APG cases. This choice leads to identical inflow conditions in the two simulations in terms of the mean velocity profile and also the inflow turbulence which is discussed below. In this manner, any changes in the transition mechanism can be attributed to the development of the boundary layer in response to the pressure gradient, rather than any differences at the inlet. The same approach was adopted in previous studies, for example the work by Nolan & Zaki (2013).

During the flow simulation, a time sequence of three-dimensional instantaneous flow fields $\boldsymbol{U}_{DNS}(x, y, z, t)$ was stored. The time interval between two consecutive samples is two time units with a total of 4000 and 8000 samples stored for the APG and ZPG cases, respectively. Furthermore, a spanwise and temporal mean velocity field $\bar{\boldsymbol{u}}$ is computed for all streamwise and wall-normal grid locations. The velocity-fluctuation field is therefore given by $\boldsymbol{u}'(x, y, z, t) = \boldsymbol{U}_{DNS}(x, y, z, t) - \bar{\boldsymbol{u}}(x, y)$.

The methodology for generating free-stream turbulence at the inflow plane of the computational domain was introduced by Jacobs & Durbin (2001). The perturbation field is represented by a weighted superposition of eigenfunctions of the continuous spectra of the Orr–Sommerfeld and homogeneous Squire operators. Use of the homogeneous operators is motivated by the observation that the Orr–Sommerfeld and Squire equations are decoupled outside the shear. In addition, these eigenfunctions do not exhibit the free-stream anisotropy that arises due to the particular normal vorticity in the coupled Orr–Sommerfeld/Squire system (see e.g. Schmid & Henningson 2000) and which was recently remarked by Dong & Wu (2013). In the limit $y \to \infty$, the inlet disturbance can be expressed in terms of Fourier modes,

$$v(x, y, z) = \hat{v} \exp(\mathrm{i}(k_x x + k_y y + k_z z)) \tag{2.2}$$

$$\eta(x, y, z) = \hat{\eta} \exp(\mathrm{i}(k_x x + k_y y + k_z z)). \tag{2.3}$$

The ansatz

$$\hat{v} = -\mathrm{i}\frac{Ak_{13}}{\kappa}, \quad \hat{\eta} = \mathrm{i}Bk_{13}, \tag{2.4}$$

where $k_{13} = \sqrt{k_x^2 + k_z^2}$ and $\kappa = \sqrt{k_x^2 + k_y^2 + k_z^2}$, yields the following amplitudes of the Cartesian velocity components

$$\hat{u} = \mathrm{i}\frac{Ak_xk_y}{k_{13}\kappa}\hat{v} + \frac{Bk_z}{k_{13}}\hat{\eta}, \quad \hat{w} = \mathrm{i}\frac{Ak_yk_z}{k_{13}\kappa}\hat{v} - \frac{Bk_x}{k_{13}}\hat{\eta}. \tag{2.5}$$

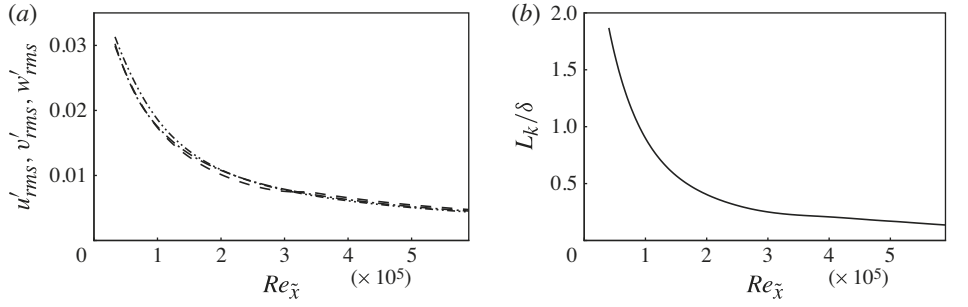

FIGURE 1. Free-stream decay of turbulence versus Reynolds number $Re_{\tilde{x}}$ (ZPG case): (*a*) r.m.s. of the velocity fluctuations, u (dashed), v (dash-dotted), w (dash-dot-dotted); (*b*) turbulence length scale.

Let further θ_1, θ_2 and δ be uniformly distributed random angles. One then arrives at a spatially isotropic perturbation field by relating the perturbation coefficients A and B to the weight function $F(\kappa)$ via

$$A = F(\kappa)\exp(\mathrm{i}\theta_1)\cos\delta, \quad B = F(\kappa)\exp(\mathrm{i}\theta_2)\sin\delta. \tag{2.6}$$

The kinetic energy of the full perturbation spectrum is hence obtained by the integral,

$$\begin{aligned} k &= \frac{1}{2}\int_0^\infty 4\pi\kappa^2(\hat{u}\hat{u}^* + \hat{v}\hat{v}^* + \hat{w}\hat{w}^*)\,\mathrm{d}\kappa \\ &= \frac{1}{2}\int_0^\infty 4\pi\kappa^2 F(\kappa)^2\,\mathrm{d}\kappa \equiv \int_0^\infty E(\kappa)\,\mathrm{d}\kappa. \end{aligned} \tag{2.7}$$

A von Kármán spectrum, where $E(\kappa)\sim\kappa^4$ for large scales and $E(\kappa)\sim\kappa^{-5/3}$ in the inertial range is obtained from the specific choice

$$E(\kappa) = Tu_{FS}^2\frac{1.196(\kappa L_{11})^4}{[0.558+(\kappa L_{11})^2]^{17/6}}L_{11}, \tag{2.8}$$

where Tu_{FS} is the turbulence intensity in the free stream, and L_{11} describes the peak of the energy spectrum. Throughout this work, values of $Tu_{FS} = 3\%$ and $L_{11} = 1$ are used.

The downstream evolution of root-mean-square (r.m.s.) of the three Cartesian components of the free-stream perturbation field is provided in figure 1(*a*). A near-isotropic, exponential decay is observed. The downstream evolution of the integral length scale

$$L_k = -\frac{k^{3/2}}{\mathrm{d}k/\mathrm{d}x}, \tag{2.9}$$

normalized by the local boundary-layer thickness, is shown in figure 1(*b*).

The downstream development of the skin friction coefficient is presented in figure 2(*a*). For the ZPG boundary layer, fully turbulent flow is observed for Reynolds numbers higher than 4×10^5. In the presence of the APG, the flow becomes turbulent at $Re_{\tilde{x}}\approx 2\times10^5$.

Breakdown to turbulence is preceded by the formation of boundary-layer streaks which are dominated by the streamwise velocity component. Therefore, u'_{rms} is often

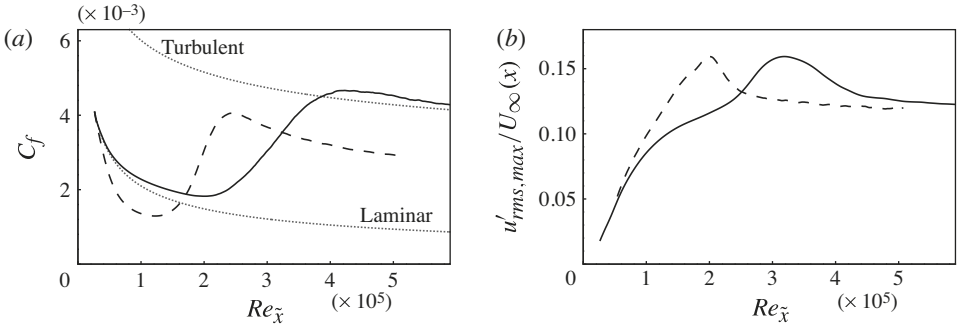

FIGURE 2. (*a*) Skin friction coefficient C_f versus Reynolds number $Re_{\tilde{x}}$; (*b*) maximum r.m.s. of the streamwise velocity fluctuation $u'_{rms,max}$ inside the boundary layer versus Reynolds number $Re_{\tilde{x}}$. The solid line represents the ZPG case, the dashed line represents the APG case.

reported as a measure of the streak amplitude. The wall-normal maximum in u'_{rms} is plotted versus downstream Reynolds number in figure 2(*b*). The observed peak values are 16% of the free-stream velocity for both flow configurations. In the APG case, this maximum is nonetheless reached substantially farther upstream than in the ZPG boundary layer.

2.2. *Instability analysis*

The linear stability analysis of a base state extracted from DNS flow fields follows the approach described by Barkley & Henderson (1996) and Barkley, Blackburn & Sherwin (2008). The eigensolver in the present work, however, is a more flexible scheme which efficiently computes eigenvalues that match a prescribed phase speed as well as of those that are most unstable (see appendix A).

Two-dimensional instantaneous velocity fields are extracted from the stored DNS snapshots $\boldsymbol{Q}_{DNS} = (U, V, W, P)^{\mathsf{T}}_{DNS}$ in planes normal to the downstream coordinate x while freezing the solution time t. The dependence of the base flow in the stability analysis on x and t is therefore parametric, and each analysis corresponds to a fixed set of values for these coordinates. This simplification can be substantiated by the weak time-dependence of the pretransitional base flow which is a superposition of the steady boundary layer and low-frequency streaks. The parallel flow assumption is further justified by the range of Reynolds numbers, $Re_\delta \in [1200, 3000]$, and the high frequency of the secondary instability modes. In primitive variables, the base state of the stability analysis becomes $\boldsymbol{Q}_{stab}(y, z; x, t) = (U, V, W, P)^{\mathsf{T}}_{stab} = (U(x, y, z, t)_{DNS}, 0, 0, 0)^{\mathsf{T}}$.

The secondary instability is described by the state vector $\boldsymbol{q}_2 = (\boldsymbol{u}_2, p_2)^{\mathsf{T}}$, with $\boldsymbol{u}_2 = (u_2, v_2, w_2)^{\mathsf{T}}$. A normal mode assumption is invoked in the streamwise direction,

$$\boldsymbol{q}_2(x, y, z, t) = \hat{\boldsymbol{q}}_2(y, z, t)\exp(\mathrm{i}\alpha x), \tag{2.10}$$

where α is a parameter of the calculation. The linearized stability equations can be written as

$$\frac{\partial}{\partial t}\hat{\boldsymbol{u}}_2 = -\mathrm{i}\boldsymbol{L}\hat{\boldsymbol{u}}_2, \tag{2.11}$$

with

$$\boldsymbol{L} = \mathrm{i}\left[\left(\nabla\boldsymbol{\Delta}^{-1}\nabla^{\mathsf{T}} - \boldsymbol{I}\right)\left(\left(\boldsymbol{U}^{\mathsf{T}}_{stab}\nabla\right) + \left(\nabla\boldsymbol{U}^{\mathsf{T}}_{stab}\right)^{\mathsf{T}}\right) + \frac{1}{Re}\nabla^2\right]. \tag{2.12}$$

Here, $\boldsymbol{\Delta}^{-1}$ is the formal inverse of the Laplacian. The time evolution of the perturbation field is then formally described by

$$\hat{\boldsymbol{u}}_2(t) = \boldsymbol{A}(t)\hat{\boldsymbol{u}}_2(0), \tag{2.13}$$

with the fundamental solution operator $\boldsymbol{A}(t)$. Differentiation of (2.13) with respect to time yields

$$\frac{\partial}{\partial t}\boldsymbol{A} = -\mathrm{i}\boldsymbol{L}\boldsymbol{A} \quad \text{with initial condition } \boldsymbol{A}(0) = \boldsymbol{I}, \tag{2.14}$$

which has the formal solution $\boldsymbol{A}(t) = \exp(-\mathrm{i}\boldsymbol{L}t)$.

The eigenspectrum of $\boldsymbol{A}$ gives information about the modal stability of the underlying base flow $\boldsymbol{U}_{stab}$, since the time evolution of the eigenfunctions of $\boldsymbol{A}$ is governed by the exponential law $\hat{\boldsymbol{u}}_2(t) = \hat{\boldsymbol{u}}_2(0)\exp(-\mathrm{i}\sigma t)$. The real part of the complex quantity σ provides the modal frequency, and its imaginary part gives the temporal growth rate of the disturbance. Since the operator $\boldsymbol{L}$ is non-diagonal, an explicit construction of $\boldsymbol{A}$ from the matrix exponential is numerically expensive and is thus avoided. Instead, a subspectrum of the fundamental solution operator is approximated using an adaptation of the implicitly restarted Arnoldi (IRAM) scheme introduced by Sorensen (1992): see appendix A.

The boundary conditions for the velocity field of the secondary instabilities are the impermeability condition at the wall and zero stress at the top of the domain,

$$u_2, v_2, w_2 = 0 \quad \text{for } y = 0 \tag{2.15}$$

$$v_2, \frac{\partial u_2}{\partial y}, \frac{\partial w_2}{\partial y} = 0 \quad \text{for } y \to \infty. \tag{2.16}$$

Consistent with the DNS flow field, periodic boundary conditions are enforced in the spanwise dimension for all velocity components.

Spectral elements are employed for the spatial discretization of the stability equations in the cross-flow plane. The number of grid points is 385 in the span and 97 in the wall-normal direction of which 70 are situated below $y = 2\delta(x)$.

Even though the stability analysis considers frozen states of the base flow in planes of constant streamwise coordinate, the underlying DNS data describe the full spatiotemporal evolution of the flow field. It is thus possible to capture the downstream development of an instability mode by applying the linear analysis to a series of base states which are translated downstream with the instability as a function of time. The characteristic speed which dictates the downstream displacement of the plane of the analysis between two consecutive stability calculations is provided by the modal phase speed, $c_r = \sigma_r/\alpha$.

3. Streak instabilities

This section provides a detailed study of representative cases for an outer instability situated on a lifted low-speed streak as well as an inner mode which originates from the intersection of a low-speed and a high-speed streak. In all cases, the base flow is extracted from direct simulations of boundary layers subject to forcing with broadband vortical free-stream perturbations. In addition to investigating the properties of streak instabilities in a realistic representation of a pretransitional boundary layer, an important second objective of this section is to establish whether linear instability analysis can accurately capture the properties of the streak instabilities observed in direct simulations. Therefore, characteristics of the secondary instabilities are

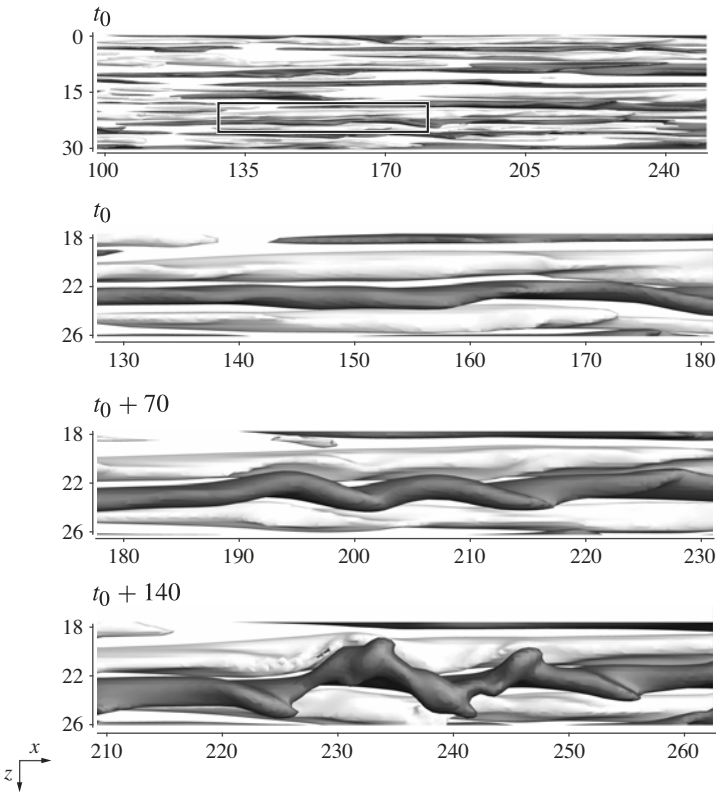

FIGURE 3. Time sequence of an outer instability observed in DNS; plan view with isosurfaces of high-speed ($u' = 0.085$, light) and low-speed streaks ($u' = -0.085$, dark).

identified in the DNS flow fields, and directly compared with the results obtained from linear instability analyses.

3.1. *Instability of lifted low-speed streaks: the outer mode*

Outer modes originate from the shear between the free stream and lifted low-speed streaks. This section discusses a sample case of breakdown to turbulence via the formation of an outer mode observed in a ZPG boundary layer subject to broadband free-stream vortical perturbations.

A time sequence of a lifted low-speed streak undergoing a sinuous instability is provided in figure 3. Regions of constant negative and positive streamwise velocity fluctuation are shown as dark and bright surfaces, respectively. The top frame depicts the entire flow field which includes a spectrum of streaks over its transverse extent. The remaining frames focus on a particular streak that develops a secondary instability and ultimately breaks down to turbulence. In order to follow the instability, the frame shown is translated downstream with the phase speed of the mode, $c_r = 0.76$.

The instability becomes manifest in a streamwise undulation of the base streak which is antisymmetric with respect to the centre line of the streak. The streamwise extent of the instability is nonetheless significantly shorter than the length of the underlying streak. This localized nature of the instability persists until breakdown to turbulence. As a consequence, a spatially isolated spot forms which is both preceded

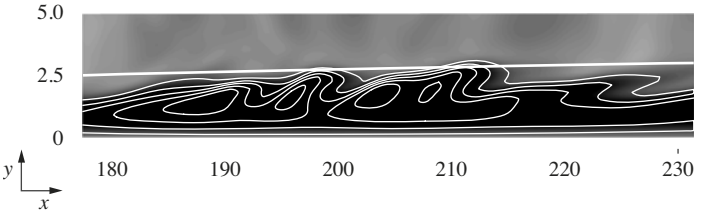

FIGURE 4. Side view of the streak developing a sinuous outer instability at $t = t_0 + 70$, $z = 22.6$; contours of the streamwise velocity fluctuation, $-0.12 \leqslant u' \leqslant 0.12$. Dark contours are negative and light contours are positive values. The thick white line marks the local boundary-layer thickness.

and succeeded by the laminar streak. Similar breakdown scenarios were reported in the experimental studies of Matsubara & Alfredsson (2001) and Asai *et al.* (2007), which indicates that breakdown was induced by an outer mode in those cases as well.

In order to elucidate the origin of the streak instability, the flow field at time $t_0 + 70$ (second frame in figure 3) is more closely inspected. A plane at the constant transverse position $z = 22.6$, at the centre of the low-speed streak is shown in figure 4. The low-speed streak is seen to occupy the largest part of the boundary layer. The region of the streak that develops the instability, $x \approx 150$, is near the edge of the boundary layer. This observation is consistent with the general description of the outer instability by Vaughan & Zaki (2011, see their figure 29). However, that work only considered idealized streaks which develop due to forcing by monochromatic vortical modes. Therefore, their streaks were repeated in the span, and the instability was subharmonic in that dimension. In the present case, on the other hand, the free-stream forcing is broadband and thus the resulting streaks are less regular. In addition, the secondary instability is localized: an important distinction that cannot be gleaned from the side view in figure 4.

Top views of the wall-normal and spanwise velocity perturbations at $t_0 + 70$ are shown in figure 5. The planes are located at $y/\delta(x) = 0.8$. The instability is evident in both the v' and w' contours. The wall-normal fluctuation shows a spanwise antisymmetric pattern with similar positive and negative peaks. In contrast to v', the spanwise velocity perturbation is symmetric with respect to the centreline of the streak. The streamwise phase of w' is shifted downstream by a quarter of a wavelength when compared with v'. The streamwise extent of the instability in figure 5 comprises approximately two to two-and-half periods, $N = 2$–2.5, at this time instance. Inspections of time series indicate that N increases during the amplification of the instability and, at the time of breakdown to turbulence, the instability typically comprises three streamwise periods. These results are consistent with the findings by Lundell (2004) who destabilized streaks using acoustic forcing with different values of N. That work concluded that N has a substantial influence on the growth rate of the streak instability, and the maximum growth rate was recorded for $N = 2.5$.

In order to investigate the stability of the base flow, a plane is extracted at $x = 155$ from the DNS flow field and a linear stability analysis is performed as described in § 2.2. The solution time is t_0, corresponding to the two topmost frames of figure 3. The temporal growth rate of the most unstable mode is $\sigma_i = 0.033$ and the modal phase speed is $c_r = 0.76$ in units of the inlet boundary-layer thickness δ_0 and the free-stream velocity U_∞. A visualization of the streamwise component of the instability eigenfunction is provided in figure 6. Solid contour lines mark positive

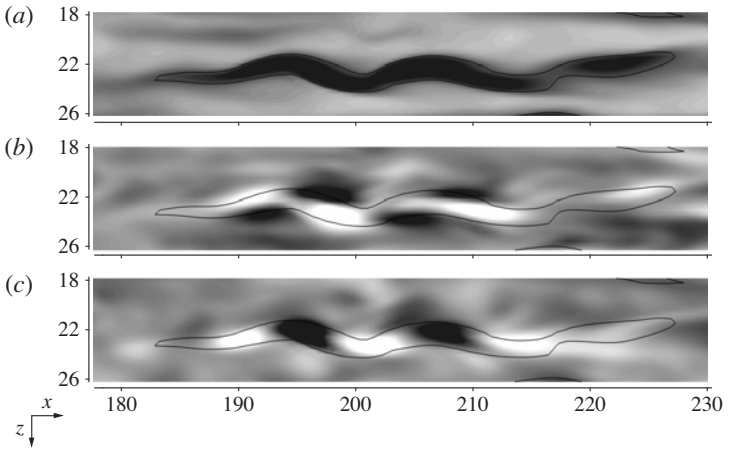

FIGURE 5. Plan view of a sinuous outer streak instability from DNS at $y/\delta(x) \approx 0.80$ and $t = t_0 + 70$. Contours of (*a*) streamwise ($-0.15 \leqslant u' \leqslant 0.15$), (*b*) wall-normal ($-0.025 \leqslant v' \leqslant 0.025$) and (*c*) spanwise ($-0.040 \leqslant w' \leqslant 0.040$) velocity fluctuations. Dark contours are negative and light contours are positive values. Solid lines mark $u' = -0.085$.

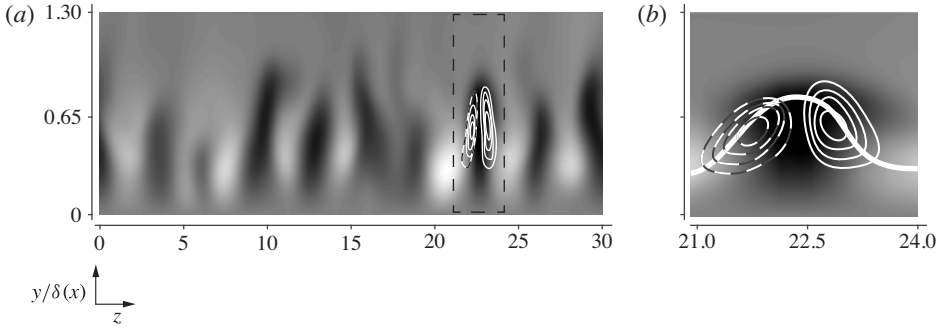

FIGURE 6. Real part of the streamwise component of the eigenfunction of an outer mode at $x = 155$, $t = t_0$. Solid lines denote positive u_2 and dashed lines are negative values. Grey contours: streamwise velocity fluctuation ($-0.25 \leqslant u' \leqslant 0.25$). (*a*) Full spanwise extent of the computational domain. (*b*) Enlarged view. The thick white line marks the critical layer.

u_2, and dashed lines mark negative u_2. The background colour gives the streamwise fluctuation field u'. Figure 6(*a*) shows the full spanwise extent of the computational domain. The eigenfunction is centred around the particular low-speed streak located at $z \approx 23$ which was observed in the time sequence from the DNS (figure 3) to undergo breakdown via a sinuous instability. The zoomed-in view provided in figure 6(*b*) shows that the mode is antisymmetry with respect to the base streak. Similar mode shapes had been reported for the sinuous mode in the studies of idealized streaks by Andersson *et al.* (2001) and Vaughan & Zaki (2011). However, unlike their spanwise subharmonic streak instability, the current eigenfunction is clearly localized on the single most unstable streak.

The three velocity components of the instability eigenfunction are shown in figure 7. Light (dark) isosurfaces denote a positive (negative) real part. One and a half streamwise wavelengths of the mode are visualized, where all lengths are

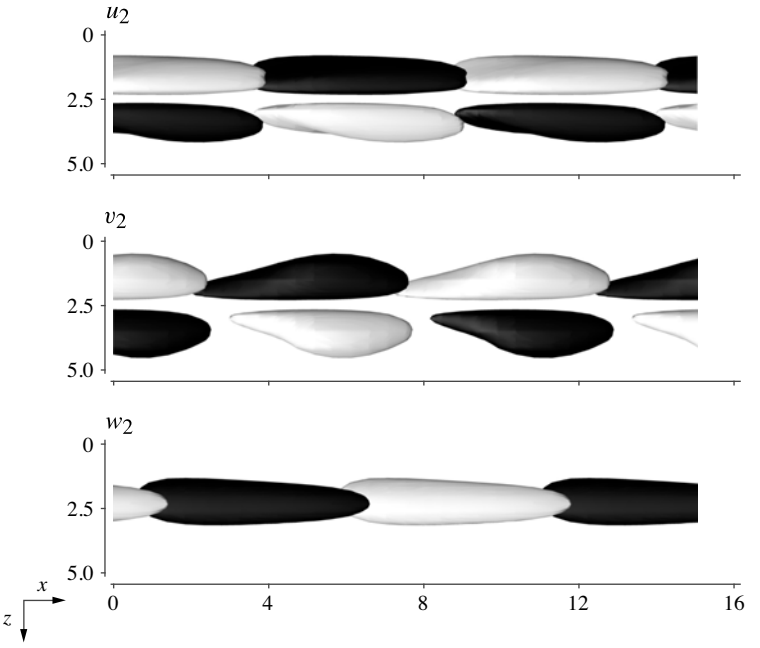

FIGURE 7. Real part of the eigenfunction of an outer mode computed for $x = 155$, $t = t_0$; three-dimensional plan view with isosurfaces of positive (white) and negative (black) real part of u_2, v_2 and w_2.

normalized by the inlet boundary-layer thickness. One may thus directly compare the shape of the eigenfunctions to the instability in the perturbation fields in figure 5. The instability mode indeed exhibits the spanwise antisymmetric and symmetric patterns for the wall-normal and spanwise velocity, respectively, as observed in the DNS. The peak amplitude of w_2 is approximately 1.8 times that of v_2, both in the nonlinear simulations and in the eigenfunction obtained from the secondary instability analysis.

In order to evaluate the changes to the secondary instability mode as it evolves downstream, the plane of the instability analysis is translated downstream with the flow. It is important to recall, however, that the instability analysis is inherently limited to the computation of purely temporal growth at any given downstream position. The convective effect and the associated downstream increase in Reynolds number during the evolution of the instability are only taken into account by conducting a series of analyses and translating the plane of the analysis downstream with the flow as a function of time. Starting from the above-presented instance ($x = 155$, $t = t_0$), the stability analysis is repeated at upstream positions at earlier times as well as at downstream planes at later times. The plane of the analysis is translated at the phase speed of the mode $\Delta t = \Delta x/c_r$, see §2.2. In general, the streamwise extent over which a unique instability can be computed is restricted. The identification of the mode fails at some upstream point where the corresponding base streak has not yet developed a sufficiently large magnitude to support the instability. At large downstream distances, the notion of the secondary instability analysis becomes ambiguous once the magnitude of the instability becomes appreciable and the base streak becomes visibly distorted. In the present case, the streamwise range of the linear analysis was $x \in [115, 190]$.

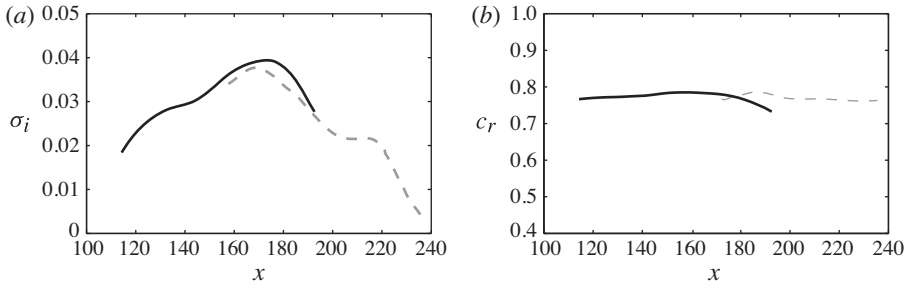

FIGURE 8. (*a*) Growth rate σ_i of an outer mode as a function of the downstream coordinate x, computed from linear analysis (solid) and extracted from DNS data (dashed). (*b*) Phase speed c_r of an outer mode as a function of the downstream coordinate x, computed from linear analysis (solid) and extracted from DNS data (dashed).

The modal growth rates evaluated from the linear analysis and extracted from the DNS fields are compared in figure 8(*a*). The former (solid line) increases up to a peak value of $\sigma_i \approx 0.04$ at $x = 175$, followed by a sharp drop near the region where the growing amplitude of the streak deformation prevents the further pursuit of the instability. The phase speed obtained by linear analysis (solid line in figure 8(*b*)) is relatively insensitive to the downstream coordinate, $c_r \sim 0.78$. Similar values have been reported by Andersson *et al.* (2001) and Vaughan & Zaki (2011) for the outer mode.

For comparison, characteristics of the streak instabilities were extracted directly from the DNS data. The spanwise velocity perturbation was used. The local extrema of w' observed in figure 5(*c*) are tracked in space and time as the secondary instability develops. Their separation defines the streamwise wavelength of the secondary instability, and the phase speed is evaluated from the mean rate of change of their downstream positions. Similar to the approach adopted by Lundell (2004), the magnitude of the extrema, $A_{w'}$, is used to compute the exponential growth rate of the instability,

$$\sigma_i = \frac{1}{\Delta t} \ln \left(\frac{A_{w'}(t + \Delta t)}{A_{w'}(t)} \right). \tag{3.1}$$

Free-stream perturbations entering the boundary layer nonetheless cause a certain degree of background noise. As a consequence, the definite identification of the instability wave requires the latter to have amplified to a minimum magnitude of approximately 1% of the free-stream velocity, effectively imposing a limit on how far upstream the instability properties can be evaluated directly from DNS data. The streamwise overlap between DNS and linear results is thus limited, but nonetheless sufficient to compare the results (figure 8). A very good agreement in the growth rate is observed between DNS and linear theory. This outcome is unexpected since the growth rate in the DNS is spatiotemporal while that from linear analysis is purely temporal.

The growth rates of the outer mode are substantially higher than those of the TS wave. For example, for a Blasius base state, $\sigma_{i,TS} = 4 \times 10^{-4}$ $(x = 100)$ and $\sigma_{i,TS} = 3 \times 10^{-3}$ $(x = 350)$.

The streamwise wavenumber, α, of the instability mode is a parameter of the linear analysis, and its influence on the growth rate is presented in figure 9(*a*). The dashed line corresponds to $x = 120$, and the solid line shows the result at $x = 175$. The peaks of both curves approximately coincide at $\alpha \approx 0.65$. In the DNS (figure 5),

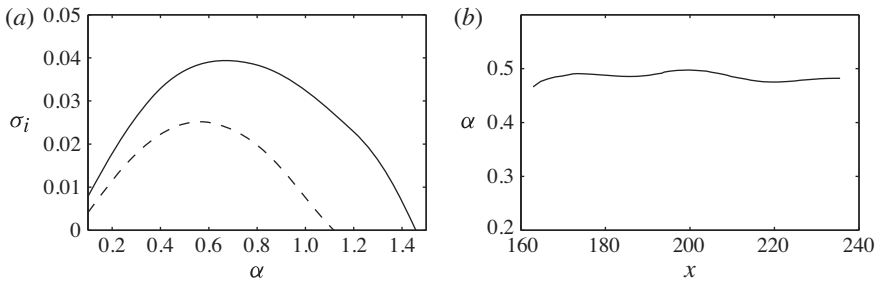

FIGURE 9. (*a*) Temporal growth rate σ_i of the instability mode as a function of the streamwise perturbation wavenumber α for $x = 125$ (dashed) and $x = 175$ (solid). (*b*) Streamwise wavenumber α of the instability as a function of the downstream coordinate x (DNS data).

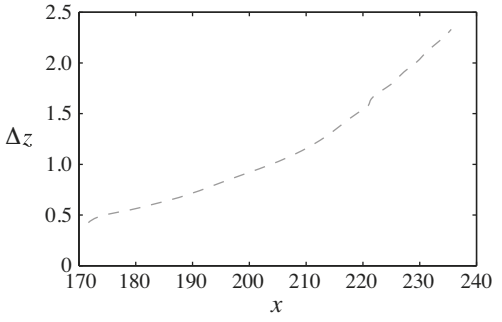

FIGURE 10. Spatial amplitude Δz of the streak distortion as a function of the downstream coordinate x.

the streamwise wavenumber of the mode can be obtained from the streamwise distance between local extrema of w', and is presented in figure 9(*b*). The observed wavenumber range of $\alpha \in [0.47, 0.50]$ is in good agreement with the highest amplified α predicted by linear theory.

DNS visualizations of u' (figure 3) show a downstream increase in the transverse deformation of the streak, Δz, by the secondary instability. The development of Δz is evaluated from the spanwise positions of the extrema in w', and is plotted in figure 10. An exponential growth rate of approximately 0.027 is obtained, which is on the same order as the above reported growth rate from linear theory.

Earlier studies have demonstrated that both the amplitude and the profile of the base streak can influence the growth rate of the secondary instabilities (e.g. Vaughan & Zaki 2011). The current streak amplitude, u'_{streak}, is shown in figure 11; here, u'_{streak} is defined as the peak value of u' along the streak of interest. The initially flat curve indicates that the streak amplitude is saturated during the interval where the secondary instability was evaluated. Therefore, the reported change in the growth rate (figure 8) is not due to a variation in the streak amplitude, but rather due to changes in the streak profile in the cross-stream plane. Since the outer mode only becomes unstable above a critical streak amplitude, an initial stage exists prior to the region reported in figures 8 and 11 where the growth rate crosses the stability boundary with increasing u'_{streak}. Once the streak amplitude saturates, the growth rate continues to change due to the variation in the base streak profile.

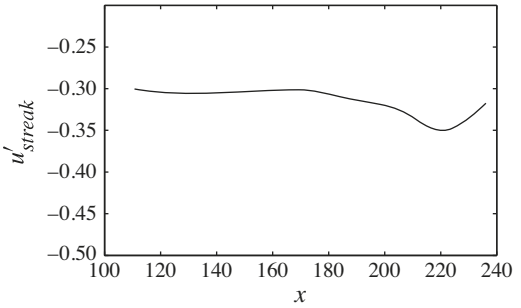

FIGURE 11. Base streak magnitude u'_{streak} versus downstream coordinate x.

The vortical structure associated with the outer instability mode is visualized using the λ_2 criterion introduced by Jeong & Hussain (1995). Isosurfaces of $\lambda_2 = -0.003$ were evaluated at time $t = t_0 + 70$ (see figure 12). The vortex core is located at the centre of the lifted low-speed streak. In addition, the streamwise extent of the vortex structure approximately matches that of the instability wave. The vortex is spanwise symmetric with respect to the underlying base streak. An inspection of the spatial structure of the vorticity eigenfunction, $\boldsymbol{\omega}_2 \equiv \boldsymbol{\nabla} \times \boldsymbol{u}_2$ (not shown) demonstrates that only the streamwise component $\omega_{x,2}$ shares this property while $\omega_{y,2}$ and $\omega_{z,2}$ are antisymmetric with respect to the transverse extent of the streak.

The decomposition of the instantaneous DNS flow field into the mean and fluctuations can be further extended into the contribution of streaks and of the instabilities,

$$\begin{aligned} \boldsymbol{U} &= \overline{\boldsymbol{u}} + \boldsymbol{u}' \\ &= \overline{\boldsymbol{u}} + \boldsymbol{u}'^{\boldsymbol{S}} + \boldsymbol{u}'^{\boldsymbol{I}}. \end{aligned} \tag{3.2}$$

The notion of streaks is herein restricted to the streamwise velocity component, i.e. $v'^S, w'^S \approx 0$ and therefore $v' \approx v'^I$, $w' \approx w'^I$. When considering the vorticity field, a similar triple decomposition applies,

$$\boldsymbol{\omega} = \overline{\boldsymbol{\omega}} + \boldsymbol{\omega}' \tag{3.3}$$

$$= \overline{\boldsymbol{\omega}} + \boldsymbol{\omega}'^{\boldsymbol{S}} + \boldsymbol{\omega}'^{\boldsymbol{I}}. \tag{3.4}$$

Since the mean flow is two-dimensional and the streaks are dominated by u', a number of simplifications are possible,

$$\omega_x = \underbrace{\overline{\omega_x}}_{=0} + \underbrace{\omega_x'^S}_{\approx 0} + \omega_x'^I \tag{3.5a}$$

$$\omega_y = \underbrace{\overline{\omega_y}}_{=0} + \omega_y'^S + \omega_y'^I \tag{3.5b}$$

$$\omega_z = \overline{\omega_z} + \omega_z'^S + \omega_z'^I. \tag{3.5c}$$

The streamwise vorticity component therefore provides a good measure of the secondary instability. Isosurfaces of ω'_x are presented in figure 13 for time $t_0 + 70$. Orange (bright) isosurfaces mark regions of positive ω'_x, and purple (dark) isosurfaces correspond to regions of negative ω'_x. The streamwise extent of the vorticity

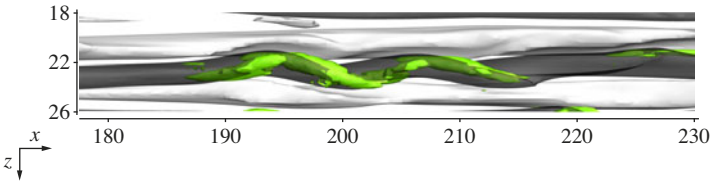

FIGURE 12. Plan view of the sinuous outer instability with isosurfaces of $\lambda_2 = -0.003$ (green) used as a vortex identification criterion for $t = t_0 + 70$.

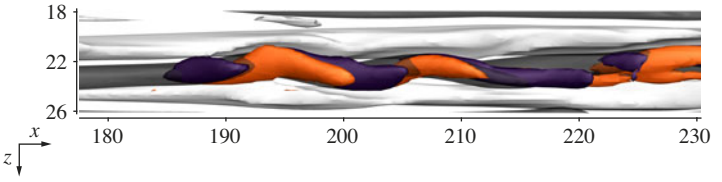

FIGURE 13. Isosurfaces of positive ($\omega_x' = 0.085$, orange/bright) and negative ($\omega_x' = -0.085$, purple/dark) streamwise vorticity. The solution time is $t = t_0 + 70$.

perturbation coincides with the location of the streak distortion. The wavelength of the vorticity isosurfaces matches that of the velocity perturbation. A closer investigation of ω_x' shows that the magnitude of $\partial w'/\partial y$ substantially outweighs that of $\partial v'/\partial z$.

The governing equation for the streamwise vorticity component is

$$\frac{\mathrm{D}\omega_x}{\mathrm{D}t} = \underbrace{\omega_x \frac{\partial U}{\partial x}}_{\textit{vorticity stretching}} \underbrace{+\omega_y \frac{\partial U}{\partial y} + \omega_z \frac{\partial U}{\partial z}}_{\textit{vorticity tilting}} + \frac{1}{Re}\nabla^2 \omega_x. \tag{3.6}$$

Owing to the inviscid nature of the instability, focus is placed only on the first three terms on the right-hand side of (3.6). An integral approach is adopted to examine the stretching and tilting terms.

The vorticity tilting and stretching terms are integrated over a volume V_{streak}, defined as the region in which the streak amplitude is greater than 1% of the free-stream velocity. The streamwise extent of the volume spans $25\delta_0$ upstream and downstream of the centre of the instability, and thus corresponds to the size of the frames shown in figure 13.

The solid line in figure 14 gives the volume integral,

$$f_1 := \frac{1}{V_{streak}} \int_{V_{streak}} \left| \omega_x \frac{\partial U}{\partial x} + \omega_y \frac{\partial U}{\partial y} + \omega_z \frac{\partial U}{\partial z} \right| \mathrm{d}V, \tag{3.7}$$

which can be interpreted as a theoretical maximum for the growth of $\int_V |\omega_x| \mathrm{d}V$. The magnitude of ω_x will intensify only if the sign of the right-hand side matches that of the local ω_x, and therefore a second measure is devised,

$$f_2 := \frac{1}{V_{streak}} \int_{V_{streak}} \frac{\omega_x}{|\omega_x|} \left(\omega_x \frac{\partial U}{\partial x} + \omega_y \frac{\partial U}{\partial y} + \omega_z \frac{\partial U}{\partial z} \right) \mathrm{d}V. \tag{3.8}$$

This quantity is the net forcing which leads to an increase of $\int_V |\omega_x| \mathrm{d}V$. Figure 14 shows that f_2 is positive throughout the amplification process of the mode and $f_2/f_1 \approx 0.60$.

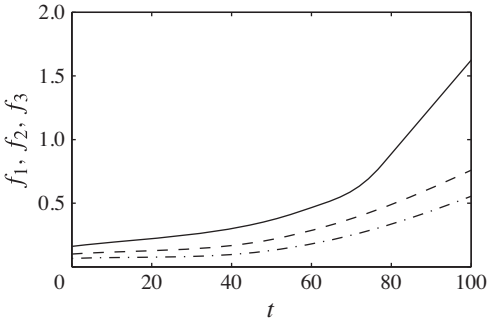

FIGURE 14. Integral vorticity forcing measures f_1 (solid), f_2 (dashed) and f_3 (dash-dotted) for the outer mode.

The relative importance of tilting and stretching is assessed by evaluating the integral of the tilting term,

$$f_3 := \frac{1}{V_{streak}} \int_{V_{streak}} \frac{\omega_x}{|\omega_x|} \left(\omega_y \frac{\partial U}{\partial y} + \omega_z \frac{\partial U}{\partial z} \right) \mathrm{d}V. \tag{3.9}$$

Figure 14 shows that the tilting term contributes approximately 70% of the total generation of ω_x.

The tilting term is further expanded as

$$\omega_y \frac{\partial U}{\partial y} + \omega_z \frac{\partial U}{\partial z} = \left(\frac{\partial U}{\partial z} - \frac{\partial W}{\partial x} \right) \frac{\partial U}{\partial y} + \left(\frac{\partial V}{\partial x} - \frac{\partial U}{\partial y} \right) \frac{\partial U}{\partial z} \tag{3.10}$$

$$= \underbrace{-\frac{\partial W}{\partial x} \frac{\partial U}{\partial y}}_{T_y} + \underbrace{\frac{\partial V}{\partial x} \frac{\partial U}{\partial z}}_{T_z}. \tag{3.11}$$

The wall-normal tilting term, T_y, is nearly an order of magnitude larger than the spanwise counterpart, T_z. The dominance of the wall-normal term is also apparent in visualizations of isosurfaces of T_y (figure 15(*a*,*b*), respectively). The streamwise vorticity $\omega_x'^I$ of the outer mode is therefore a result of the meandering of the unstable streak $\partial W/\partial x$ and the wall-normal shear in the base state $\partial U/\partial y$.

3.2. *Instability of streak intersections: the inner mode*

The inner mode was first computed by Vaughan & Zaki (2011) in the case of idealized streaks. Their Floquet analysis predicted a spanwise fundamental secondary instability, with a critical layer close to the wall and a phase speed approximately half the free-stream velocity. The present study of transition beneath free-stream turbulence shows that localized instabilities, which can be classified as inner modes, arise due to the local shear between low- and high-speed streaks. Configurations in which the trailing edge of a high-speed streak is situated on top of a low-speed streak lead to highly inflectional velocity profiles in the wall-normal direction. The presence of an APG further promotes this effect. In that case, the majority of breakdowns are initiated by an inner instability (§4). In the present section, breakdown via an inner mode is investigated in an APG boundary layer characterized by a Hartree parameter $\beta_H = -0.14$.

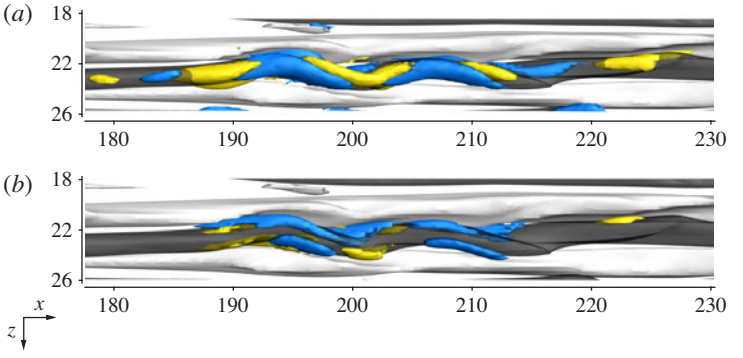

FIGURE 15. Isosurfaces of streamwise velocity perturbation (white, $u' = 0.085$; grey, $u' = -0.085$) and vorticity tilting terms (blue, $T_{y,z} = 0.002$; yellow, $T_{y,z} = -0.002$). (*a*) Wall-normal term T_y. (*b*) Spanwise term T_z. The solution time is $t = t_0 + 70$.

A visualization of a streak configuration that leads to breakdown via amplification of a varicose inner instability is provided in figure 16. Isosurfaces of positive (light) and negative (dark) u' are shown in the plan view. The topmost frame shows the whole spanwise extent of the flow field. The magnified views in the remaining frames show the time evolution of the particular streak that breaks down to turbulence. The downstream position of the frames is translated with the phase speed of the instability. Even though the streaks appear undistorted in the top frame, results from linear stability analysis presented below show that the growth rate of the instability has already reached a substantial magnitude. The streak subsequently develops a streamwise pattern of local contractions which precede breakdown to turbulence. In comparison with the evolution of the outer mode (figure 3), isosurfaces of u' do not provide a clear empirical view of the evolution of the inner instability.

A side view of the streamwise perturbation field u' at $z = 23.8$ is shown in figure 17. This spanwise position bisects the base streaks that develop the instability. The flow field shows a high-speed streak whose leading edge overlaps with a low-speed streak which is located close to the wall. The same flow configuration led to breakdown in the phenomenological studies by Brandt & de Lange (2008) and the DNS by Vaughan & Zaki (2011).

Contours of the velocity fluctuations in a plane located at $y/\delta(x) = 0.45$ are shown in figure 18. The shape of the wall-normal velocity perturbation is spanwise symmetric with respect to the underlying base streak and shows a shape similar to that of Λ vortices. The perturbation extends upstream in the form of two streamwise elongated legs which are situated to the left and right of the base streak. A staggered pattern with alternating patches of positive and negative velocity fluctuations is observed in the streamwise direction. The spanwise fluctuation field, on the other hand, is antisymmetric with respect to the centreline of the base streak. It also bears similarity with the wavepacket reported in the simulations of transition under the influence of a blunt leading edge by Nagarajan *et al.* (2007) and the instability analysis by Vaughan & Zaki (2011).

Linear stability analysis is applied to a base flow extracted from the DNS data in a cross-plane at $x = 103$. The solution time is t_1, which is visualized in the two topmost frames in figure 16. The streamwise component, u_2, of the most unstable eigenfunction is shown as black solid lines in figure 19(*a*). The eigenfunction is

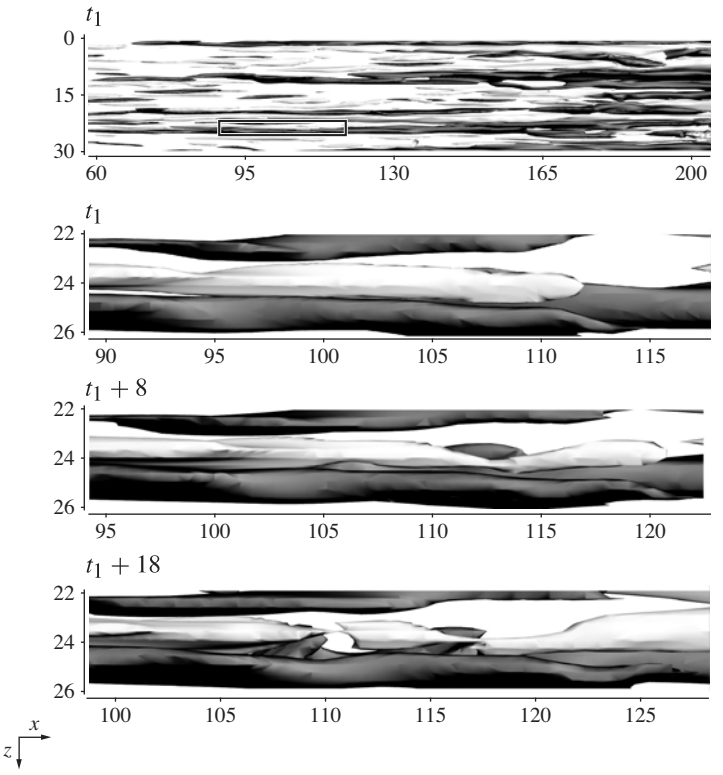

FIGURE 16. Time sequence of an inner instability from DNS; plan view with isosurfaces of high-speed ($u' = 0.085$, light) and low-speed ($u' = -0.085$, dark) streaks.

centred around the particular streak which, further downstream in the DNS, exhibits a clear instability and ultimately induces breakdown to turbulence. The zoomed-in view in figure 19(*b*) shows that the mode is spanwise symmetric with respect to the base streak. The growth rate and phase speed of the mode are $\sigma_i = 0.08$ and $c_r = 0.54$, respectively.

Similar to the outer mode, the eigenfunction of the inner streak instability is centred around its critical layer. An inviscid analysis in the limit $Re \to \infty$ recovers the same eigenmode as viscous stability theory, which supports the view that the mode is a Rayleigh-type instability (see the dotted lines in figure 19(*b*)). The phase speed of the inviscid mode, $c_{r,inviscid} = 0.54$, matches that of the viscous analysis. However, the inviscid stability analysis over-predicts the growth rate, $\sigma_{i,inviscid} = 0.12$.

The spatial structure of the eigenfunction of the most unstable mode is visualized over one and a half streamwise wavelengths in figure 20. A spanwise symmetric structure is observed for the streamwise component u_2 of the instability eigenfunction, which reflects the varicose deformation of the base streak seen in figure 16. The wall-normal component v_2 has a staggered pattern with small streamwise legs, similar to the wall-normal fluctuation field v' of the DNS (see figure 18(*a*)). A similar agreement is observed for the antisymmetric pattern of the spanwise component w_2.

The inner mode in the time series (figure 16) amplifies rapidly and induces breakdown over a downstream distance of $30\delta_0$. As a consequence, the streamwise extent over which the mode can be tracked by means of both instability analysis and

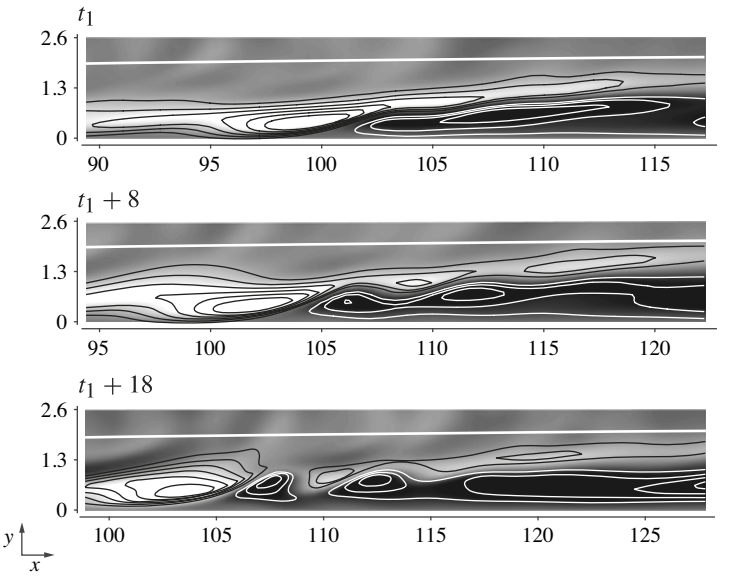

FIGURE 17. Side view of the streak configuration leading to the formation of a varicose inner instability at $z = 23.8$, $t = t_1$. Contours of the streamwise velocity fluctuation, $-0.12 \leqslant u' \leqslant 0.12$. The thick white line marks the edge of the boundary layer.

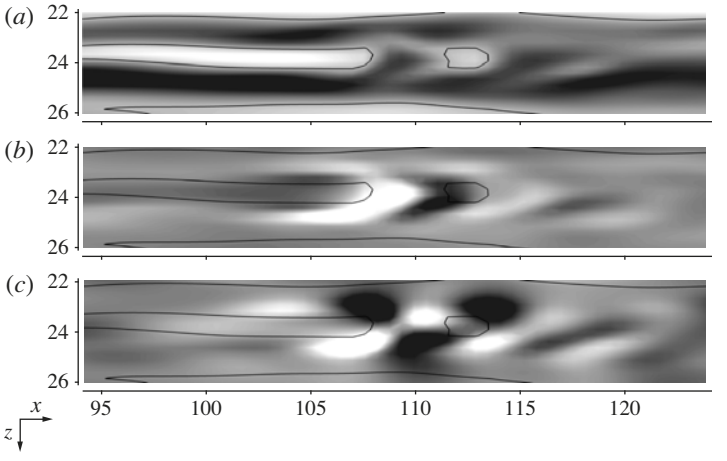

FIGURE 18. Plan view of a varicose inner streak instability from DNS at $y/\delta(x) \approx 0.45$, $t = t_1 + 18$. Contours of (*a*) streamwise ($-0.17 \leqslant u' \leqslant 0.17$), (*b*) wall-normal ($-0.025 \leqslant v' \leqslant 0.025$) and (*c*) spanwise ($-0.025 \leqslant w' \leqslant 0.025$) velocity fluctuations. Solid black lines mark $u' = 0.085$.

the post-processing of DNS flow fields is substantially shorter than that of the outer mode. The previously mentioned restrictions still apply: the identification of the mode in the DNS requires a certain minimum amplitude; and the instability analysis fails once the modal amplitude becomes substantial in the base state.

The eigenvalue of the mode computed in the linear analysis is given by the solid line in figure 21(*a*). The growth rate σ_i increases from the start of the analysis at

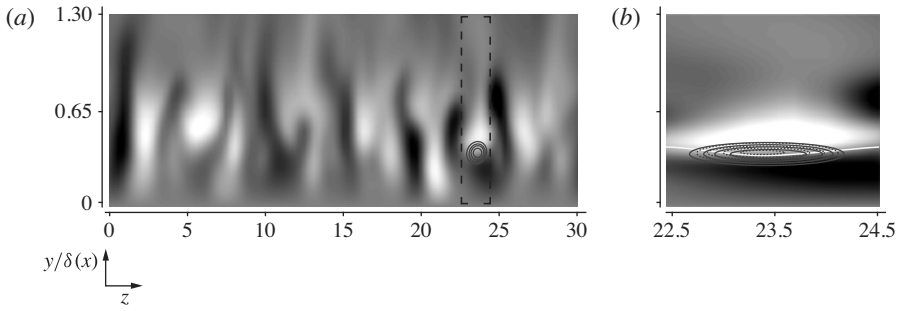

FIGURE 19. Real part of the streamwise component of the eigenfunction of an inner mode for u_2 (solid lines) computed at $x = 103$, $t = t_1 + 18$. Black dotted lines mark contours of $u_{2inviscid}$ computed in the inviscid limit. Grey contours: streamwise velocity fluctuation ($-0.17 \leqslant u' \leqslant 0.17$). (*a*) Full spanwise extent of the computational domain. (*b*) Detailed view. The thick white line marks the critical layer.

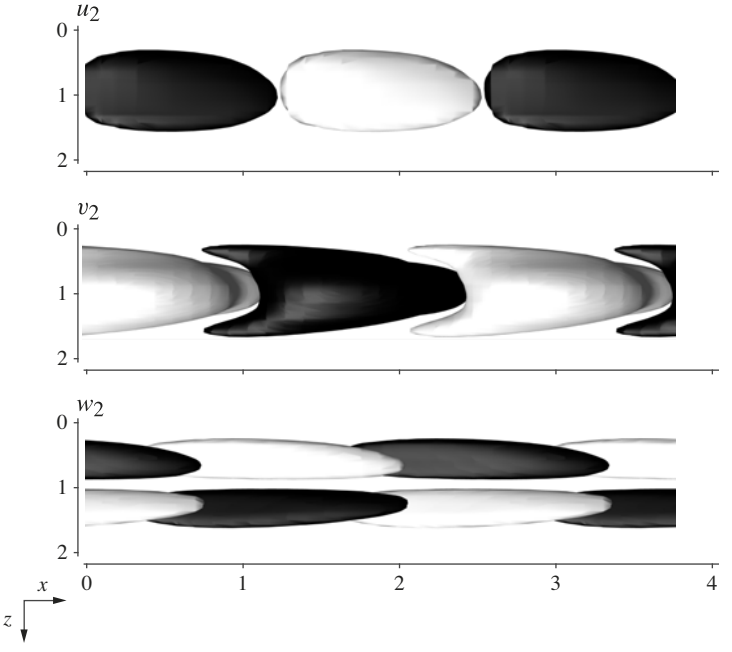

FIGURE 20. Eigenfunction of an inner mode computed for $x = 103$, $t = t_1 + 18$; three-dimensional plan view with isosurfaces of positive (white) and negative (black) real part of u_2, v_2 and w_2.

$x \approx 87$ until a peak is reached approximately at the downstream location where the amplitude of the streak distortion becomes appreciable. This behaviour is qualitatively similar to what had been observed for the outer mode. The magnitude of the growth rate in the present case is nonetheless substantially higher. The temporal growth rate computed from DNS flow fields is given by the dashed line in figure 21(*a*). The downstream locations of the peak growth rates of both approaches approximately coincide. The magnitude of the growth rate computed from the DNS data is however

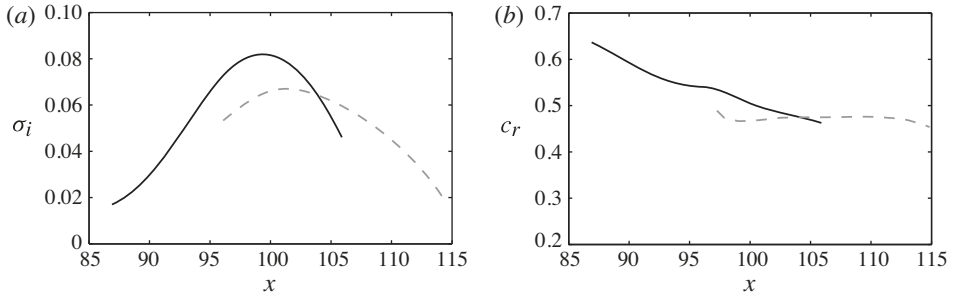

FIGURE 21. (*a*) Growth rate σ_i of an inner mode as a function of the downstream coordinate x computed from linear analysis (solid) and extracted from DNS data (dashed). (*b*) Phase speed c_r of an inner mode as a function of the downstream coordinate x computed from linear analysis (solid) and extracted from DNS data (dashed).

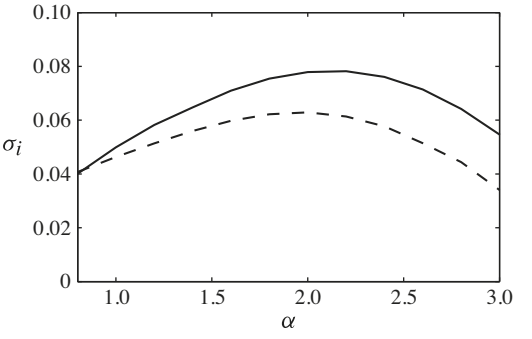

FIGURE 22. Temporal growth rate σ_i of the instability mode as a function of the streamwise perturbation wavenumber α for $x = 95$ (dashed) and $x = 104$ (solid).

20% smaller than the linear result. In this context, it should be re-emphasized that, even though applied at different downstream positions, the linear analysis provides a purely temporal growth rate. The DNS data on the other hand inherently capture the full spatiotemporal evolution.

The phase speeds are presented in figure 21(*b*). The stability analysis indicates a continuous decrease in the phase speed from approximately $c_r = 0.63$ to $c_r = 0.47$. Further downstream, a direct evaluation of the DNS flow field yields a nearly constant phase speed of $c_r \approx 0.48$. It is instructive to compare the growth rate of the secondary instability to that of the most unstable mode of the base flow, in the absence of free-stream turbulence. Owing to the APG, the mean velocity profile is inflectional and can support inviscid Rayleigh-type instability. For the relevant downstream range, $50 < x < 200$, the growth rate increases from $\sigma_{i,Ray} = 0.019$ to $\sigma_{i,Ray} = 0.023$. While significantly exceeding the growth rates of TS waves reported in the previous section, these values are still smaller than those for the inner mode reported in figure 21(*a*).

Figure 22 shows the dependence of the growth rate from linear theory on the streamwise wavenumber α. The highest amplified wavelengths at $x = 95$ and $x = 104$ coincide at $\alpha \approx 2.2$. This wavelength approximately matches that observed in the DNS flow field.

The origin of the inner mode was stated earlier to be in the shear between low- and high-speed streaks. An investigation of the influence of the streak amplitude on

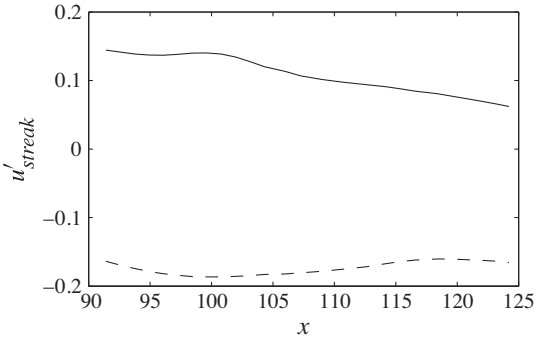

FIGURE 23. Amplitude u'_{streak} of the high-speed (solid line) and low-speed (dashed line) streaks as a function of the downstream coordinate x.

the growth rate of the inner instability must therefore take into account both streaks. The peak amplitudes of the low- and high-speed streaks are presented in figure 23 versus downstream distance. The amplitudes of both streaks are significantly lower than that of the low-speed streak associated with the outer mode that was discussed in the previous section. These observations are consistent with the result by Vaughan & Zaki (2011) who reported that the threshold amplitude for streak instability is lower for the inner mode.

In order to investigate the vortex structures associated with the inner mode, the λ_2 vortex identification criterion is applied. Isosurfaces of $\lambda_2 = -0.003$ are shown in figure 24. The solution time is $t_1 + 18$, which corresponds to the third frame in figure 16. Streamwise-elongated vortices are observed along the flanks of the high-speed streak, connected through an arch which is situated on top of the streak near $x \simeq 110$. This Λ-shaped structure is fundamentally different from the vortical structures seen in the case of the outer mode.

Similar to the outer mode, the streamwise component of the vorticity eigenfunction $\boldsymbol{\omega}_2$ computed by linear stability analysis matches the spatial structure of the vortex. A visualization of the streamwise vorticity fluctuation taken from DNS data is provided in figure 25(a). Isosurfaces of positive and negative ω'_x are shown. A comparison with the vortical structures identified in figure 24 indeed shows that the legs of the Λ vortices coincide with locations of high ω'_x. The spatial distribution of the latter is spanwise antisymmetric with respect to the base streak with alternating patches of positive and negative vorticity.

4. Statistical results

The characteristics of canonical examples of an outer- and an inner-streak instability were discussed in detail in §3. In this section, these findings are complemented by statistical data from the investigation of a large number of unique streak instabilities. The characteristic properties of the instabilities are computed via linear analysis only, an approach that is justified by the good quantitative agreement with DNS demonstrated earlier. The results are separately reported for ZPG and APG boundary layers, with a focus on the respectively prevailing type of streak instability. §4.1 is devoted to the analysis of outer modes in ZPG boundary layers while §4.2 covers inner modes in APG boundary layers. A direct comparison between the growth rates of inner and outer modes is presented in §4.3.

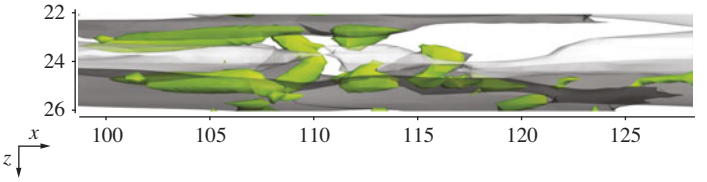

FIGURE 24. Plan view of the varicose inner instability with isosurfaces of $\lambda_2 = -0.003$ (green) used as a vortex identification criterion for $t = t_1 + 18$.

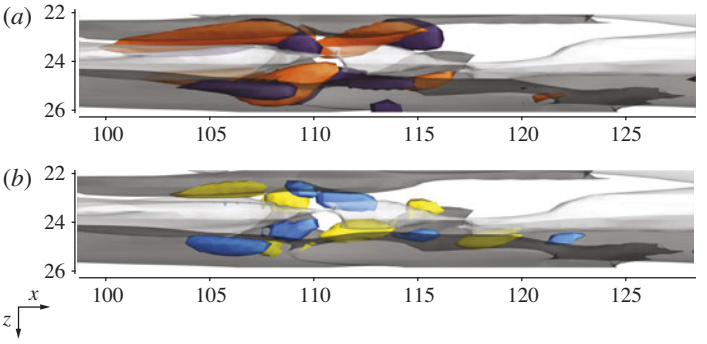

FIGURE 25. (*a*) Isosurfaces of positive ($\omega_x' = 0.085$, orange/bright) and negative ($\omega_x' = -0.085$, purple/dark) streamwise vorticity. (*b*) Isosurfaces of positive ($\mathrm{D}\omega_x'/\mathrm{D}t = 0.002$, yellow/bright) and negative ($\mathrm{D}\omega_x'/\mathrm{D}t = -0.002$, blue/dark) material derivative of streamwise vorticity. The solution time is $t = t_1 + 18$.

4.1. *ZPG boundary layer*

For the ZPG boundary layer, a total of 102 unique breakdown events has been investigated, with breakdown defined as the formation of an isolated turbulent spot which is in all spatial dimensions surrounded by laminar flow. Of these breakdowns, 80 were preceded by the formation of an outer instability situated on top of a lifted low-speed streak. The remaining 22 breakdowns were either of a different type (e.g. inner modes) or were inaccessible to an investigation by means of linear analysis, and have thus been excluded from the data presented herein. The remaining set of outer instabilities can be further separated into 73 sinuous and 7 varicose modes.

In all cases, the downstream position x and solution time t of the linear instability analysis were chosen relative to the corresponding breakdown event. The inception location of the turbulent spot is determined using the laminar/turbulent flow discrimination method described by Nolan & Zaki (2013).

It was mentioned earlier that the stability analysis is only meaningful in a window where the base streak has reached high amplitude but where the secondary instability itself does not yet measurably deform the streak. Parameter studies demonstrated that an interval of 100 time units before spot inception falls into this window for the majority of outer modes. This value was consequently used for all analyses presented herein. So as to account for the initially unknown phase speed of the instability, the analysis was performed at three different downstream locations. Planes normal to the streamwise coordinate are extracted 60, 70 and 80 inlet boundary-layer thicknesses upstream the location of spot inception, corresponding to a theoretical phase speed of $c_r = \{0.60, 0.70, 0.80\}$. Owing to the localized nature of the streak

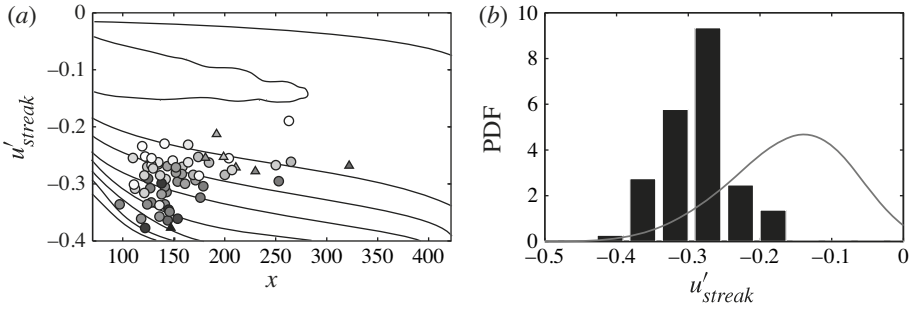

FIGURE 26. (*a*) Downstream position x of the secondary instabilities and local amplitude of their respective base streak u'_{streak}. Each data point identifies a unique streak instability with circles denoting sinuous and triangles varicose outer modes. The symbol colour is darker for higher growth rates. Lines give the local PDF of the base streak amplitude. (*b*) PDF of the base streak amplitude u'_{streak} for the streaks that develop an outer mode (bars) and for all streaks in the downstream range $x \in [100, 300]$ (line).

instability, in the majority of investigated cases only one of these locations yielded an eigenfunction representative of the instability that further downstream initiates breakdown to turbulence.

The modal growth rates of all computed outer instabilities are presented in figure 26(*a*). Each data point in the scatter plot corresponds to a unique instability; circles denote sinuous and triangles denote varicose outer modes. Instabilities represented by darker symbols have a higher growth rate. In general, streaks with high magnitudes $|u'_{streak}| > 0.30$ lead to the formation of more unstable modes.

In order to separately quantify the dependence of the modal growth rate on downstream location and the base streak magnitude, the normalized correlation coefficient

$$\rho_{a,b} := \frac{\overline{\boldsymbol{a}\ \boldsymbol{b}}}{\sqrt{\overline{\boldsymbol{a}^2}\ \overline{\boldsymbol{b}^2}}} \tag{4.1}$$

is evaluated. Here, $\overline{\boldsymbol{a}\ \boldsymbol{b}}$ denotes the covariance of the vectors $\boldsymbol{a}$ and $\boldsymbol{b}$, and the denominator is the product of their respective standard deviations. In the present case, the correlation coefficient between the magnitude of the base streak and the modal growth rate is $\rho_{|u'_{streak}|,\sigma_i} = 0.658$, indicating an appreciable influence of the streak magnitude on the growth rate of the instability. The correlation between downstream distance and modal growth rate on the other hand is very weak, with a correlation coefficient $\rho_{x,\sigma_i} = 0.183$. A similar value $\rho_{Re,\sigma_i} = 0.194$ is obtained when replacing x with the Reynolds number based on the boundary-layer thickness. The weak dependence on Reynolds number is due to the inviscid nature of the instability.

A probability density function (PDF) of the magnitudes of the base streaks, independent of their downstream position, is provided in figure 26(*b*). Bars correspond to the set of low-speed streaks which develop secondary instabilities. The distribution is centred around a value of $u'_{streak} \approx -0.30$. Similar findings for the magnitudes of streaks upstream the formation of turbulent spots had been reported in experiments by Nolan, Walsh & McElligot (2010) and in DNS studies by Nolan & Zaki (2013). The present results further indicate positive growth rates for streak amplitudes of more than 17%, which coincides with the critical streak amplitude reported in the Floquet studies of Vaughan & Zaki (2011).

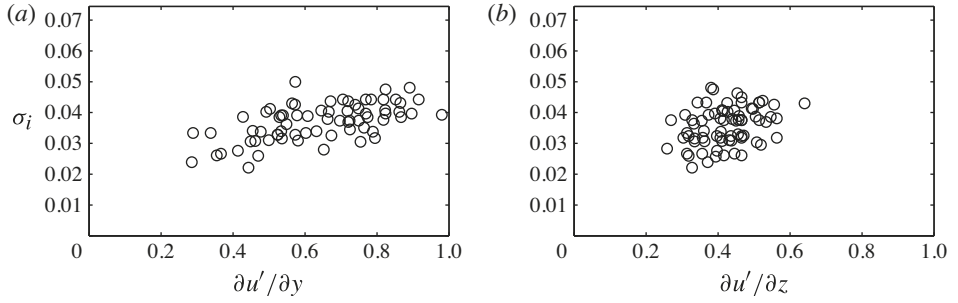

FIGURE 27. (*a*) Growth rate σ_i versus the magnitude of the maximum wall-normal shear $\partial u'/\partial y$ along the critical layer. (*b*) Growth rate σ_i versus the magnitude of the maximum spanwise shear $\partial u'/\partial z$ along the critical layer. Circles represent sinuous outer modes. Each data point identifies a unique streak instability.

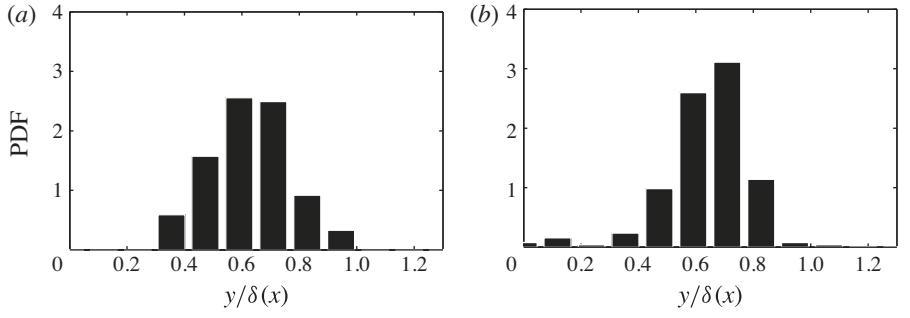

FIGURE 28. (*a*) PDF of the wall distance y of the peak magnitude of the streamwise component u_2 of the instability eigenfunction. (*b*) PDF of the wall distance y of spot inception.

It is further of interest to compare the particular streaks that develop instabilities and lead to breakdown with the full spectrum of boundary-layer streaks. The solid line in figure 26(*b*) gives the PDF of the magnitudes of all low-speed streaks that are observed in the downstream range $100 \leqslant x \leqslant 330$. The peak of this curve is located around $u'_{streak} \approx -0.12$. By integrating the PDF, it is found that the majority (80%) of breakdown events are due to base streaks with amplitudes $|u'_{streak}| \geqslant 0.25$, and that only 15% of the entire streak population fall into this group. It is therefore only a small subset of streaks that contribute significantly to the onset of turbulence in bypass transition.

The literature on Görtler vortices relates sinuous and varicose secondary instabilities to inflectional spanwise and wall-normal u profiles. In order to investigate the relationship between the local shear and the amplification of the outer mode, the maxima in $\partial u'/\partial y$ and $\partial u'/\partial z$ are extracted along the critical layers of the modes. Owing to the small number of varicose samples, only sinuous modes are taken into account. In order to exclude the influence of the Blasius boundary layer, the shear is computed from the perturbation velocity u'. Scatter plots for the modal growth rate σ_i versus $\partial u'/\partial y$ and $\partial u'/\partial z$ are provided in figure 27. These results will be compared with the inner instability in the next section (§4.2).

A PDF of the wall distance of the maximum u_2 of the instability eigenfunction is provided in figure 28(*a*). The majority of the modes are situated at a wall distance

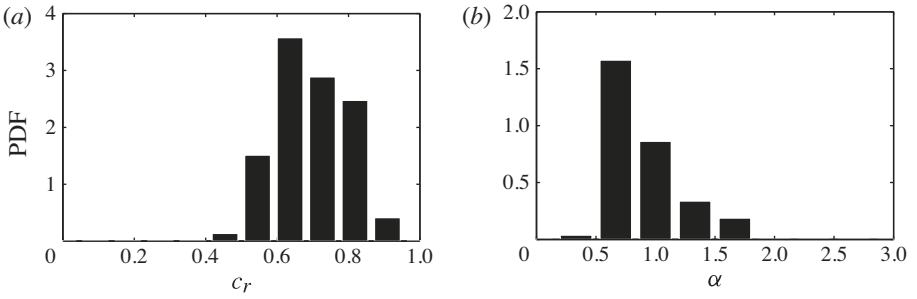

FIGURE 29. (*a*) PDF of the phase speed c_r of the streak instability. (*b*) PDF of the streamwise wavenumber α of the streak instability.

of 60–70% of the local boundary-layer thickness. This result is consistent with the terminology 'outer modes', since they are located on top of lifted low-speed streaks. Figure 28(*b*) presents a PDF of the wall-normal location of initial spot inception during the entire time series of the ZPG simulation. A clear correlation to the wall-normal location of the outer instability is seen in the figure.

A PDF of the modal phase speed of the outer modes is presented in figure 29, and demonstrates that the majority of these modes indeed propagate at 60–80% of the free-stream velocity. This compares favourably with values of $0.70U_\infty$ found by Brandt *et al.* (2004) and $0.75U_\infty$ reported by Vaughan & Zaki (2011).

It was mentioned earlier that the streamwise wavenumber α is an input parameter of the stability calculations. The PDF shown in figure 29 considers the value of α which yields the highest growth rate for each streak instability. The peak of the distribution is located at values of $\alpha \approx 0.40$, which corresponds to a streamwise wavelength $\lambda_x \approx 16$. Starting from its peak, the distribution gradually decays towards higher wavenumbers while dropping sharply to zero for smaller α.

4.2. *APG boundary layer*

This section reports statistical results for a boundary layer subject to an APG with Hartree parameter $\beta_H = -0.14$. A total of 56 unique breakdowns has been investigated, 36 of which were inner modes. The remaining 20 instabilities were either of a different type (e.g. outer modes) or could not be evaluated by means of linear analysis. Of the 36 breakdowns due to inner modes, 31 were of varicose nature with the remaining 5 showing a sinuous configuration. In contrast to the predominantly sinuous outer mode, the frequency of occurrence of the varicose inner modes is significantly higher than that of sinuous configurations.

Similar to the ZPG case, the solution time and downstream position of the instability analysis are determined relative to the position of spot inception. In order to account for the faster growth of the inner mode, the interval between the stability computation and first occurrence of a turbulent spot is reduced to 67 time units. Again, three different downstream locations are investigated, located 27, 33 and 40 inlet boundary-layer thicknesses upstream the point of spot inception. The covered range of theoretical phase speeds thus is $c_r = \{0.40, 0.50, 0.60\}$.

A scatter plot showing the dependence of the instability growth rate on streak amplitude and downstream position is provided in figure 30(*a*). Since the investigated modes arise between high- and a low-speed streaks, each instability is represented

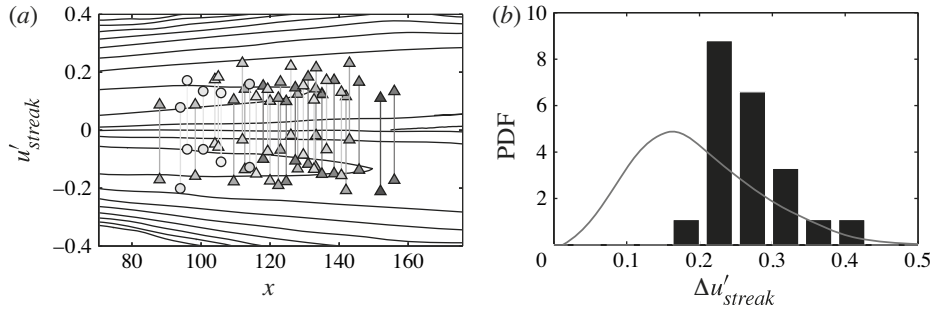

FIGURE 30. (*a*) Downstream location x and intensity of the positive and negative base streaks u'_{streak}. Each connected set of data points identifies a unique streak instability. Circles and triangles represent sinuous and varicose inner modes, respectively. The background contour lines give the PDF of the local amplitude for all high-speed and low-speed streaks. (*b*) PDF of the difference in streak magnitude $\Delta u'_{streak}$ for the pairs of streaks that lead to the formation of inner modes (bars) and for all streak intersections in the downstream range $x \in [100, 160]$ (line).

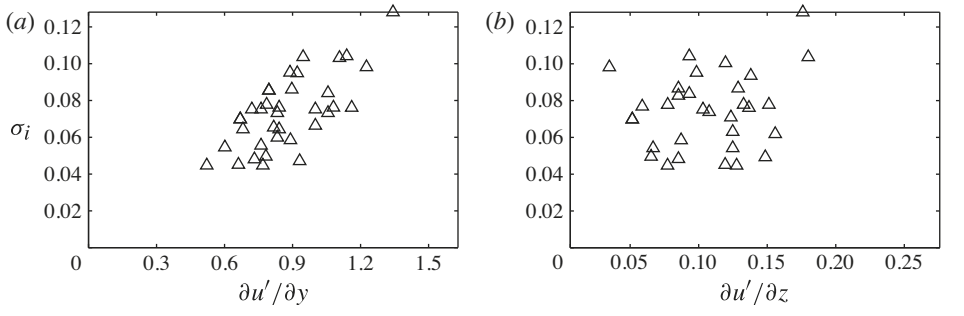

FIGURE 31. (*a*) Growth rate σ_i versus the magnitude of the maximum wall-normal shear $\partial u'/\partial y$ along the critical layer. (*b*) Growth rate σ_i versus the magnitude of the maximum spanwise shear $\partial u'/\partial z$ along the critical layer. Triangles represent varicose inner modes. Each data point identifies a unique streak instability.

by two symbols which show the respective magnitudes of these streaks. A PDF of the difference in amplitude $\Delta u'_{streak}$ between the high- and low-speed streak of each inner mode is given in figure 30(*b*). The distribution has its peak between 20 and 30% of the free-stream velocity. The solid line gives the distribution of $\Delta u'_{streak}$ for all observed streak intersections in the full time series of the APG case. Two observations are noteworthy: first, the unstable streak configurations have $\Delta u'_{streak}$ larger than the mean value; second, integration of the area under the curve shows that approximately half of all streak intersections may lead to the amplification of an instability. However, it should be noted that this overlapping low- and high-speed streak configuration only occurs in 8.4% of the total population of streaks.

Figure 31 shows the relation between the shear due to boundary-layer streaks and the growth rate of the instabilities. Data points represent the maximum values of $\partial u'/\partial y$ and $\partial u'/\partial z$ along the critical layer of the instability. A correlation coefficient of $\rho^{APG}_{\partial u'/\partial y, \sigma_i var} = 0.784$ demonstrates a nearly linear dependence of the growth rate of the varicose mode on the wall-normal shear at its critical layer. However, the modal

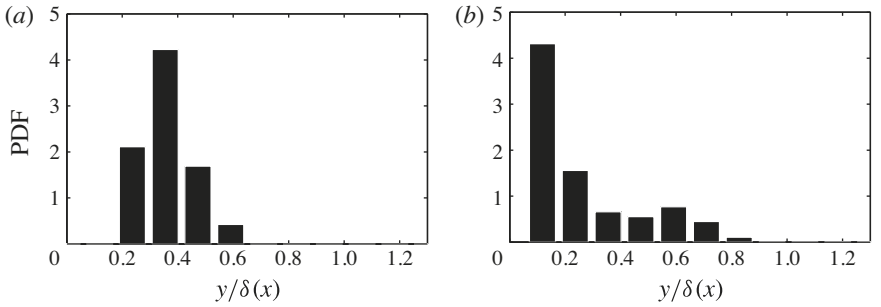

FIGURE 32. (*a*) PDF of the wall distance y of the peak magnitude of the streamwise component u_2 of the instability eigenfunction. (*b*) PDF of the wall distance y of spot inception.

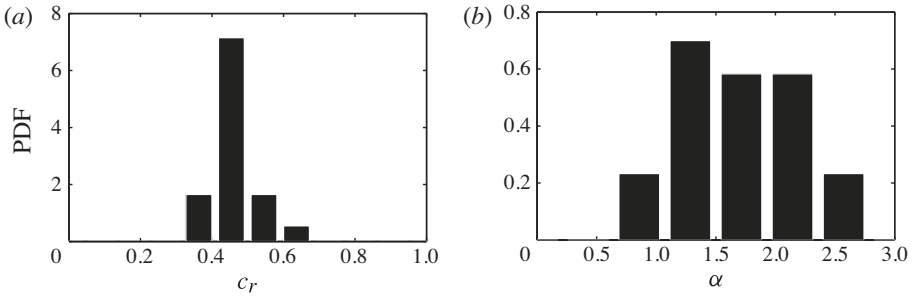

FIGURE 33. (*a*) PDF of the phase speed c_r of the streak instability. (*b*) PDF of the streamwise wavenumber α of the streak instability.

growth rate of the varicose modes is nearly uncorrelated with the spanwise shear, $\rho^{APG}_{\partial u'/\partial z,\sigma_i var} = 0.278$. Furthermore, $\partial u'/\partial z$ in the case of the varicose inner modes is nearly three times smaller than that for the sinuous outer modes (see figure 27).

The term inner modes refers to the instability being situated relatively close to the wall. A PDF of the wall distance of the peak of the streamwise component u_2 of the instability eigenfunction is presented in figure 32. Accordingly, more than 90% of the inner modes are indeed located in the lower half of the boundary layer. Figure 32(*b*) provides the wall distance of spot inception for the entire time series in the DNS, and shows that the majority of breakdowns occur within $y \leqslant 0.30\delta(x)$. Direct comparison with the results for spot inception in the ZPG case (cf. figure 28(*b*)) shows a clear shift towards smaller wall distances in the APG flow. This shift was first reported by Nolan & Zaki (2013), and is herein explained in terms of the dominance of the outer instability in ZPG and the inner mode in APG.

A PDF of the phase speed of the inner modes is presented in figure 33(*a*). A relatively narrow distribution is observed with nearly all investigated samples located in a window at 50% of the free-stream velocity. Evaluations for the outer mode presented in the previous section (cf. figure 29(*a*)) show that the majority of the outer modes have a phase speed in excess of $0.60U_\infty$. The distribution of the most unstable streamwise wavenumber of the inner modes is reported in figure 33(*b*). The wavenumber range is $1.0 \lesssim \alpha \lesssim 2.2$. Direct comparison with the results for the outer mode indicates an appreciable shift towards higher wavenumbers.

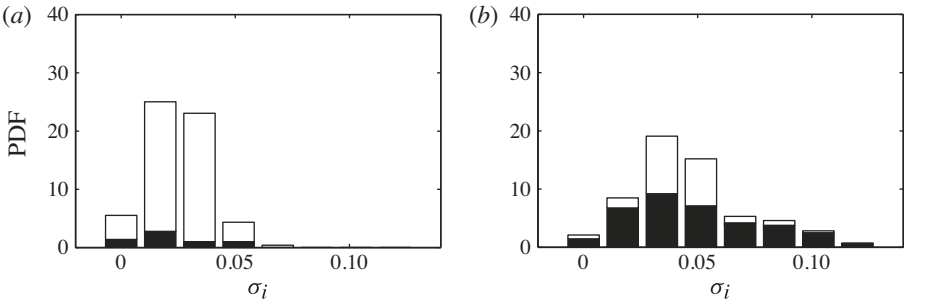

FIGURE 34. Growth rate σ_i of the most unstable eigenfunction: outer (white) and inner (black) modes. (*a*) ZPG case. (*b*) APG case.

4.3. *Competition between outer and inner modes*

The studies of bypass transition conducted by Jacobs & Durbin (2001) indicated that breakdown in ZPG boundary layers is in the majority of cases preceded by an outer instability. The results presented here confirm this view. Assuming that the amplitude of the instability at time t is given by $\|\boldsymbol{u}_2(t)\| = \|\boldsymbol{u}_2(0)\| \exp(\sigma_i t)$, two explanations for the described behaviour are possible:

(*a*) the amplitude of the initial condition $\|\boldsymbol{u}_2(0)\|$ is larger for the outer mode than for the inner mode;

(*b*) the growth rate σ_i of outer modes is generally higher than that of the inner mode in ZPG.

From a physical point of view, (*a*) relates to the flow receptivity to external perturbations and (*b*) relates to the nature of the secondary instability of the streaky boundary layer.

In the previous sections (§§4.1 and 4.2), secondary instability analyses were performed ahead of spot inception at three upstream planes. Only the mode with the largest growth rate among all three planes of investigation was retained since it identified the unstable streak that led to spot formation. In this section, the most unstable mode (optimized over all α) from each of the three planes is included in the statistics. As such, instabilities that have large growth rates, but do not induce breakdown to turbulence, be it due to their small initial amplitude or other effects, are included in the statistic.

For the ZPG boundary layer, a total of 296 samples were investigated. In 265 of these cases, the most unstable eigenfunction was an outer streak instability. The remaining 31 instabilities, equivalent to 10% of all modes, were of the inner type. A PDF of the growth rate of the most unstable mode is provided in figure 34(*a*). The black portion of each bar denotes the contribution of inner modes and the white portion denotes the contribution of outer modes. The most unstable mode is indeed of outer type. This result establishes that the current ZPG boundary layer is inherently more susceptible to outer instabilities, and breakdown is therefore more likely near the edge of the boundary layer: a likelihood potentially augmented by the free-stream forcing.

When turning to the APG case, previous results clearly demonstrated an increased relevance of the inner mode. Since shear sheltering favours the seeding of outer instabilities, the importance of the inner mode can only be explained in terms

of an increase in the growth rate. Following the same approach as in the ZPG case, the stability results of all downstream locations of all time instances are again counted as separate samples. Of the computed 165 instabilities, 95 are of the inner type and 70 are of the outer type. A PDF of the growth rate is provided in figure 34(*b*). Accordingly, the most unstable modes are predominantly of the inner type. Furthermore, the growth rates of these modes significantly exceed the maximum growth rates observed in the ZPG case (see figure 34(*a*)). It can therefore be concluded that APG substantially promotes the amplification of inner instabilities.

5. Conclusion

Linear stability analysis was applied to DNS flow fields of a boundary layer exposed to moderate levels of free-stream turbulence. The broadband vortical forcing from the free-stream turbulence leads to the generation of a spectrum of streaks inside the boundary layer. Two configurations of boundary-layer streaks often become hosts for localized, secondary instabilities: (i) the intersection of high-speed and low-speed streaks within the boundary layer; and (ii) low-speed streaks, which are lifted towards the free stream. Detailed studies show that these instabilities, despite their localized nature, can be ascribed to the general classification of inner and outer modes introduced by Vaughan & Zaki (2011).

It was shown that two-dimensional linear analyses, applied to cross-sections of the flow field, can predict the secondary instability substantially upstream of where it can be clearly identified in the DNS fields. In the stability analysis, the most unstable eigenfunction is localized around one particular streak in the base state. The same streak in the DNS will indeed, at a later time and farther downstream, develop a secondary instability and become a site for the onset of breakdown to turbulence. It was further possible to track the mode as it evolves downstream. A quantitative comparison with data computed from DNS time series showed good agreement with the growth rates and phase speeds from linear theory. The spatial structure of the eigenfunction further matches that of the instability pattern identified in the DNS data.

The evolution of a typical outer mode situated on top of a lifted low-speed streak was investigated in detail. The spatial structure of the mode leads to the streamwise meandering appearance of the host streak. Statistical evaluations showed that the magnitude of the base streak which leads to outer instabilities is between 20 and 35% of the free-stream speed. In addition, the wall-normal position of the peak in the eigenfunction for the outer mode is in good agreement with the location of turbulent spot inception in the ZPG boundary layer.

An example of an inner instability which arises in the overlap region between a low- and a high-speed streak was also discussed in detail. The inner mode is predominantly varicose. Its growth is accompanied by the formation of characteristic hairpin vortices that extend along the flanks of the base streak. Statistical evaluations showed an appreciable correlation between the growth rate of the varicose inner mode and the wall-normal shear along its critical layer.

A direct comparison of the growth rates of inner and outer modes finally showed that the most unstable mode in a ZPG boundary layer is of outer type in 90% of all cases. The prevalence of outer modes in the ZPG case is thus primarily a property of the linear stability of the streaky boundary layer. This bias changes in favour of the inner mode if an APG is applied, and the instability growth rate in also increased appreciably. These results are in agreement with the locations of spot inception recorded from the DNS flow fields.

The ability of linear analysis to accurately capture the secondary instabilities of realistic flow fields can be beneficial in a variety of scenarios. These include computational techniques that can model the amplification of streaks but not their secondary instability, for example the boundary region equations (Leib, Wundrow & Goldstein 1999). In experiments, the instability analysis may be applied to two-dimensional velocity fields obtained, for instance, by PIV in order to explain empirical observations. In the context of flow control, the analysis can identify the most unstable streaks as a candidate for actuation downstream of the measurement location. The methodology can also be applied to examine new mechanisms of breakdown such as the nonlinear optimal initial conditions in the studies by Cherubini *et al.* (2010, 2011).

Appendix A. Eigenvalue solver

In order to efficiently compute a subspectrum of $\boldsymbol{A} \in \mathbb{C}^{n\times n}$, a sequence of $j = \{1, \ldots, k\}$ orthogonal bases $\boldsymbol{V}_j := [\boldsymbol{v}_1, \boldsymbol{v}_2, \ldots, \boldsymbol{v}_j] \in \mathbb{C}^{j\times n}$ is constructed from the repeated application of $\boldsymbol{A}$ to a random start vector $\boldsymbol{v}_1$,

$$\boldsymbol{h}_j = \boldsymbol{V}_j^{\mathsf{H}} \boldsymbol{A}\boldsymbol{v}_j \tag{A 1}$$

$$\boldsymbol{f}_j = \boldsymbol{A}\boldsymbol{v}_j - \boldsymbol{V}_j\boldsymbol{h}_j \tag{A 2}$$

$$\boldsymbol{v}_{j+1} = \boldsymbol{f}_j/\|\boldsymbol{f}_j\|. \tag{A 3}$$

The first two lines of this procedure describe a classical Gram–Schmidt orthogonalization. The vector $\boldsymbol{h}$ in (A 1) is the projection of $\boldsymbol{A}\boldsymbol{v}_j$ onto the present base $\boldsymbol{V}_j$. In (A 2), the components of the base that are in the direction of $\boldsymbol{A}\boldsymbol{v}$ are subtracted from the latter. Let $\boldsymbol{H}_k := [\boldsymbol{h}_1, \boldsymbol{h}_2, \ldots, \boldsymbol{h}_k]$, then the above scheme yields the Arnoldi factorization

$$\boldsymbol{A}\boldsymbol{V}_k = \boldsymbol{V}_k\boldsymbol{H}_k + \boldsymbol{f}_k\boldsymbol{e}_k^{\mathsf{T}}, \tag{A 4}$$

where $\boldsymbol{e}_k \in \mathbb{R}^{k\times 1} = (0, \ldots, 0, 1)^{\mathsf{T}}$ is the kth unit vector. The operator $\boldsymbol{H} \in \mathbb{C}^{k\times k}$ is upper Hessenberg and hence allows the efficient computation of its eigenspectrum $\sigma(\boldsymbol{H}_k)$ through QR decomposition. The elements of this Ritz spectrum are an exact subset of the spectrum of $\boldsymbol{A}$ if and only if $\boldsymbol{f}_k = \boldsymbol{0}$. It is easily seen that this requirement is identically fulfilled if $\boldsymbol{V}_k\boldsymbol{V}_k^{\mathsf{H}}\boldsymbol{A}\boldsymbol{v}_k = \boldsymbol{A}\boldsymbol{v}_k$. In this case, $\boldsymbol{A}\boldsymbol{v}_k$ is a linear combination of the basis vectors $\boldsymbol{v}_k$, so that the columns of $\boldsymbol{V}_k$ span an invariant subspace of $\boldsymbol{A}$. Relatively large base lengths k are generally required for sufficiently small factorization residuals $\boldsymbol{f}_k$, promoting in turn high computational cost and memory requirements.

A more efficient approach is thus pursued, in which the size of k is limited by implicitly restarting the factorization once its length has reached a certain threshold (Sorensen 1992, 2002). The initial condition $\boldsymbol{v}^+$ of the restarted factorization is a combination of Ritz eigenvectors. In addition to reducing the computational requirements, this approach provides control over which part of the spectrum of $\boldsymbol{A}$ is approximated by the Ritz spectrum. In the present work, the requirement is to compute the eigenvalues that are most unstable or that most closely match a prescribed complex phase speed c_{target}. In the first case, the Ritz spectrum is sorted by the imaginary part of the eigenvalues, and in the second case by the absolute distance in the complex plane of each eigenvalue to the prescribed phase speed. The $p = m - k$, $0 < k < m$ eigenvalues that have the smallest real part or the greatest distance to c_{target} are subsequently used as shifts in a p-step Francis QR factorization

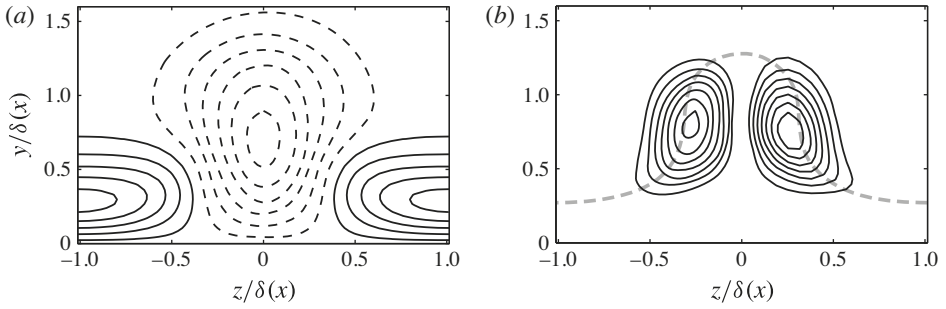

FIGURE 35. (*a*) Contours of the streamwise velocity fluctuation u' from the validation case courtesy of Dr Luca Brandt. Solid (dashed) lines denote positive (negative) fluctuations from $u' = \pm 0.035$ to $u' = \pm 0.35$ in increments of 0.063. (*b*) Contours of the absolute of the streamwise component of the instability eigenfunction from $\|u_2\| = 0.01$ to $\|u_2\| = 0.045$ in increments of 0.005. The thick dashed line marks the critical layer.

(Golub & Van Loan 1996) of $(\boldsymbol{H}_m - \mu_j \boldsymbol{I})$, $j = 1, 2, \ldots, p$, resulting in

$$\boldsymbol{A}\boldsymbol{V}_m^+ = \boldsymbol{V}_m^+ \boldsymbol{H}_m^+ + \boldsymbol{f}_m \boldsymbol{e}_m^{\mathsf{T}} \boldsymbol{Q}, \tag{A5}$$

where $\boldsymbol{V}_m^+ = \boldsymbol{V}_m \boldsymbol{Q}$, $\boldsymbol{H}_m^+ = \boldsymbol{Q}^{\mathsf{H}} \boldsymbol{H}_m \boldsymbol{Q}$ and $\boldsymbol{Q} = \boldsymbol{Q}_1 \boldsymbol{Q}_2, \ldots, \boldsymbol{Q}_p$. The $\boldsymbol{Q}_j \in \mathbb{C}^{m \times m}$ are the orthogonal operators obtained in each of the p shifted QR steps. Since $\boldsymbol{H}_m$ is Hessenberg, each $\boldsymbol{Q}_j$ inherits this property. It follows that the first $k-1$ elements of the last row of $\boldsymbol{Q}$, and thus of the vector $\boldsymbol{e}_m^{\mathsf{T}} \boldsymbol{Q}$ are zero. The first k columns of (A 5) therefore give the k-step Arnoldi factorization

$$\boldsymbol{A}\boldsymbol{V}_k^+ = \boldsymbol{V}_k^+ \boldsymbol{H}_k^+ + \boldsymbol{f}_k \boldsymbol{e}_k^{\mathsf{T}}. \tag{A6}$$

The spectrum of $\boldsymbol{H}_k^+$ now comprises the k Ritz eigenvalues that are closest to the prescribed complex phase speed. Application of another p steps (A 1)–(A 3) to (A 6) yields the next iteration of (A 5).

Appendix B. Validation of the linear stability algorithm

This section contains a validation of the numerical method used for the linear stability analyses conducted in the context of this work. As mentioned earlier, the former comprises two independent parts, namely a linear flow solver as well as the eigenvalue solver described in the previous section. It should be mentioned that both methods have been validated independently of each other. In the interest of brevity, only a combined validation of the whole numerical approach is reported here.

The base flow for the validation case has been kindly provided by Dr Luca Brandt and is identical to that used in Andersson *et al.* (2001) as well as Brandt *et al.* (2003). It describes a Blasius boundary layer distorted by a steady streak which is obtained from the nonlinear response of the boundary layer to forcing with the linearly optimal conditions calculated by Andersson *et al.* (1999). Periodicity in the spanwise dimension vindicates the limitation of the transverse extent of the computational domain to a single streak. A visualization of the streamwise velocity fluctuation u' is provided in figure 35(*a*). The peak value of u' is 35% of the free-stream velocity at the centre of the low-speed streak.

Re	σ_i Brandt *et al.* (2003)	σ_i present method	c_r present method
283	0.0518	0.0515	0.842
1415	0.0905	0.0900	0.827
5660	0.0973	0.0967	0.823

TABLE 1. Secondary instability growth rates from Brandt *et al.* (2003) as well as calculated with the present numerical method for a set of Reynolds numbers and a streamwise instability wavenumber of $\alpha = 1.70$. Data from Brandt *et al.* (2003) have been rescaled.

Contour lines of the streamwise component u_2 for the most unstable eigenfunction computed with the present method are shown in figure 35(*b*). The mode is located on top of the backward jet at the centre of the computational domain and is thus, under the terminology used throughout this work, identified as an outer instability. The shape of u_2 is antisymmetric with respect to the centreline of the base streak, indicating a sinuous type of mode. In general, the shape of the eigenfunction is in good agreement with the result presented in figure 12 of Andersson *et al.* (2001).

Brandt *et al.* (2003) computed the modal growth rate in dependence of the Reynolds number for the same base flow. Table 1 provides a comparison of their values to the results obtained with the presently employed numerical method. The relative difference in the respective modal growth rates is less than 1% in all cases.

REFERENCES

ANDERSSON, P., BERGGREN, M. & HENNINGSON, D. S. 1999 Optimal disturbances and bypass transition in boundary layers. *Phys. Fluids* **11** (1), 134–150.

ANDERSSON, P., BRANDT, L., BOTTARO, A. & HENNINGSON, D. S. 2001 On the breakdown of boundary layer streaks. *J. Fluid Mech.* **428**, 29–60.

ASAI, M., KONISHI, Y., OIZUMI, Y. & NISHIOKA, M. 2007 Growth and breakdown of low-speed streaks leading to wall turbulence. *J. Fluid Mech.* **586**, 371–396.

ASAI, M., MINAGAWA, M. & NISHIOKA, M. 2002 The instability and breakdown of a near-wall low-speed streak. *J. Fluid Mech.* **455**, 289–314.

BARKLEY, D., BLACKBURN, H. M. & SHERWIN, S. J. 2008 Direct optimal growth analysis for timesteppers. *Intl J. Numer. Meth. Fluids* **57**, 1435–1458.

BARKLEY, D. & HENDERSON, R. D. 1996 Three-dimensional Floquet stability analysis of the wake of a circular cylinder. *J. Fluid Mech.* **322**, 215–241.

BRANDT, L., COSSU, C., CHOMAZ, J.-M., HUERRE, P. & HENNINGSON, D. S. 2003 On the convectively unstable nature of optimal streaks in boundary layers. *J. Fluid Mech.* **485**, 221–242.

BRANDT, L. & DE LANGE, H. C. 2008 Streak interactions and breakdown in boundary layer flows. *Phys. Fluids* **20**, 024107.

BRANDT, L., SCHLATTER, P. & HENNINGSON, D. S. 2004 Transition in boundary layers subject to free-stream turbulence. *J. Fluid Mech.* **517**, 167–198.

BUTLER, K. M. & FARRELL, B. F. 1992 Three-dimensional optimal perturbations in viscous shear flow. *Phys. Fluids* A **4** (8), 1637–1650.

CHERUBINI, S., DE PALMA, P., ROBINET, J.-C. & BOTTARO, A. 2011 The minimal seed of turbulent transition in the boundary layer. *J. Fluid Mech.* **689**, 221–253.

CHERUBINI, S., ROBINET, J.-C., BOTTARO, A. & DE PALMA, P. 2010 Optimal wave packets in a boundary layer and initial phases of a turbulent spot. *J. Fluid Mech.* **656**, 231–259.

DONG, M. & WU, X. 2013 On continuous spectra of the Orr–Sommerfeld/Squire equations and entrainment of free-stream vortical disturbances. *J. Fluid Mech.* **732**, 616–659.

DURBIN, P. & WU, X. 2007 Transition beneath vortical disturbances. *Annu. Rev. Fluid Mech.* **39**, 107–128.

ELOFSSON, P. A., KAWAKAMI, M. & ALFREDSSON, P. H. 1999 Experiments on the stability of streamwise streaks in plane Poiseuille flow. *Phys. Fluids* **11** (4), 915–930.

FRANSSON, J. H. M., BRANDT, L., TALAMELLI, A. & COSSU, C. 2005 Experimental study of the stabilization of Tollmien–Schlichting waves by finite amplitude streaks. *Phys. Fluids* **17**, 054110.

GOLUB, G. H. & VAN LOAN, C. F. 1996 *Matrix Computations*. 3rd edn. The Johns Hopkins University Press.

GUSTAVSSON, L. H. 1991 Energy growth of three-dimensional disturbances in plane Poiseuille flow. *J. Fluid Mech.* **224**, 241–260.

HULTGREN, L. S. & GUSTAVSSON, L. H. 1981 Algebraic growth of disturbances in a laminar boundary layer. *Phys. Fluids* **24** (6), 1000–1004.

HUNT, J. C. R. & CARRUTHERS, D. J. 1990 Rapid distortion theory and the 'problems' of turbulence. *J. Fluid Mech.* **212**, 497–532.

JACOBS, R. G. & DURBIN, P. A. 1998 Shear sheltering and the continuous spectrum of the Orr–Sommerfeld equation. *Phys. Fluids* **10** (8), 2006–2011.

JACOBS, R. G. & DURBIN, P. A. 2001 Simulations of bypass transition. *J. Fluid Mech.* **428**, 185–212.

JEONG, J. & HUSSAIN, F. 1995 On the identification of a vortex. *J. Fluid Mech.* **285**, 69–94.

KIM, J. & MOIN, P. 1985 Application of a fractional-step method to incompressible Navier–Stokes equations. *J. Comput. Phys.* **59**, 308–323.

KLEBANOFF, P. S. 1971 Effect of free-stream turbulence on the laminar boundary layer. *Bull. Am. Phys. Soc.* **10**, 1323–1334.

LANDAHL, M. T. 1975 Wave breakdown and turbulence. *SIAM J. Appl. Maths* **28** (4), 735–756.

LANDAHL, M. T. 1980 A note on an algebraic instability of inviscid parallel shear flows. *J. Fluid Mech.* **98**, 243–251.

LEIB, S. J., WUNDROW, D. W. & GOLDSTEIN, M. E. 1999 Effect of free-stream turbulence and other vortical disturbances on a laminar boundary layer. *J. Fluid Mech.* **380**, 169–203.

LIU, Y., ZAKI, T. A. & DURBIN, P. A. 2008*a* Boundary-layer transition by interaction of discrete and continuous modes. *J. Fluid Mech.* **604**, 199–233.

LIU, Y., ZAKI, T. A. & DURBIN, P. A. 2008*b* Floquet analysis of secondary instability of boundary layers distorted by Klebanoff streaks and Tollmien–Schlichting waves. *Phys. Fluids* **20**, 124102.

LUCHINI, P. 2000 Reynolds-number-independent instability of the boundary layer over a flat surface: optimal perturbations. *J. Fluid Mech.* **404**, 289–309.

LUNDELL, F. 2004 Streak oscillations of finite length: disturbance evolution and growth. *Phys. Fluids* **16**, 3227–3230.

MANDAL, A. C., VENKATAKRISHNAN, L. & DEY, J. 2010 A study on boundary-layer transition induced by free-stream turbulence. *J. Fluid Mech.* **660**, 114–146.

MANS, J., KADIJK, E. C., DE LANGE, H. C. & VAN STEENHOVEN, A. A. 2005 Breakdown in a boundary layer exposed to free-stream turbulence. *Exp. Fluids* **39**, 1071–1083.

MANS, J., DE LANGE, H. C. & VAN STEENHOVEN, A. A. 2007 Sinuous breakdown in a flat plate boundary layer exposed to free stream turbulence. *Phys. Fluids* **19**, 088101.

MARQUILLIE, M., EHRENSTEIN, U. & LAVAL, J.-P. 2011 Instability of streaks in wall turbulence with adverse pressure gradient. *J. Fluid Mech.* **681**, 205–240.

MATSUBARA, M. & ALFREDSSON, P. H. 2001 Disturbance growth in boundary layers subjected to free stream turbulence. *J. Fluid Mech.* **430**, 149–168.

NAGARAJAN, S., LELE, S. K. & FERZIGER, J. H. 2007 Leading-edge effects in bypass transition. *J. Fluid Mech.* **572**, 471–504.

NOLAN, K. P., WALSH, E. J. & MCELLIGOT, D. M. 2010 Quadrant analysis of a transitional boundary layer subject to free-stream turbulence. *J. Fluid Mech.* **658**, 310–335.

NOLAN, K. P. & ZAKI, T. A. 2013 Conditional sampling of transitional boundary layers in pressure gradients. *J. Fluid Mech.* **728**, 306–339.

RICCO, P., LUO, P. & WU, X. 2011 Evolution and instability of unsteady nonlinear streaks generated by free-stream vortical disturbances. *J. Fluid Mech.* **677**, 1–38.

ROSENFELD, M., KWAK, D. & VINOKUR, M. 1991 A fractional step solution method for the unsteady incompressible Navier–Stokes equations in generalized coordinate systems. *J. Comput. Phys.* **94**, 102–137.

SCHMID, P. J. & HENNINGSON, D. S. 2000 *Stability and Transition in Shear Flows*. Springer.

SCHRADER, L.-U., BRANDT, L. & HENNINGSON, D. S. 2009 Receptivity mechanisms in three-dimensional boundary-layer flows. *J. Fluid Mech.* **618**, 209–241.

SCHRADER, L.-U., BRANDT, L. & ZAKI, T. A. 2011 Receptivity, instability and breakdown of Görtler flow. *J. Fluid Mech.* **682**, 362–396.

SORENSEN, D. C. 1992 Implicit application of polynomial filters in a k-step Arnoldi method. *SIAM J. Matrix Anal. Applics.* **13**, 357–385.

SORENSEN, D. C. 2002 Numerical methods for large eigenvalue problems. *Acta Numerica* 519–584.

SWEARINGEN, J. D. & BLACKWELDER, R. F. 1987 The growth and breakdown of streamwise vortices in the presence of a wall. *J. Fluid Mech.* **182**, 255–290.

TREFETHEN, L. N., TREFETHEN, A. E., REDDY, S. C. & DRISCOLL, T. A. 1993 Hydrodynamic stability without eigenvalues. *Science* **261** (5121), 578–584.

VAUGHAN, N. J. & ZAKI, T. A. 2011 Stability of zero-pressure-gradient boundary layer distorted by unsteady Klebanoff streaks. *J. Fluid Mech.* **681**, 116–153.

WESTIN, K. J. A., BOIKO, A. V., KLINGMANN, B. G. B., KOZLOV, V. V. & ALFREDSSON, P. H. 1994 Experiments in a boundary layer subjected to free stream turbulence. Part 1. Boundary layer structure and receptivity. *J. Fluid Mech.* **281**, 193–218.

ZAKI, T. A. 2013 From streaks to spots and on to turbulence: exploring the dynamics of boundary layer transition. *Flow Turbul. Combust.* **91**, 451–473.

ZAKI, T. A. & DURBIN, P. A. 2005 Mode interaction and the bypass route to transition. *J. Fluid Mech.* **531**, 85–111.

ZAKI, T. A. & DURBIN, P. A. 2006 Continuous mode transition and the effects of pressure gradients. *J. Fluid Mech.* **563**, 357–388.

ZAKI, T. A. & SAHA, S. 2009 On shear sheltering and the structure of vortical modes in single- and two-fluid boundary layers. *J. Fluid Mech.* **626**, 111–147.